Copyright
by
Koichi Noguchi
2001

STRUCTURE FORMATION THROUGH MAGNETOHYDRODYNAMICAL INSTABILITIES IN PROTOPLANETARY AND ACCRETION DISKS

by

KOICHI NOGUCHI, B.E., M.S.

DISSERTATION

Presented to the Faculty of the Graduate School of

The University of Texas at Austin

in Partial Fulfillment

of the Requirements

for the Degree of

DOCTOR OF PHILOSOPHY

THE UNIVERSITY OF TEXAS AT AUSTIN

May 2001

STRUCTURE FORMATION THROUGH MAGNETOHYDRODYNAMICAL INSTABILITIES IN PROTOPLANETARY AND ACCRETION DISKS

APPROVED BY
DISSERTATION COMMITTEE:

Supervisor: _____

Toshiki Tajima

_____

Roger D. Bengtson

_____

Herbert L. Berk

_____

C. Wendell Horton

_____

Paul R. Shapiro

Acknowledgements

I would like to thank my supervisor, Prof. Tajima, for his guidance over years to help my understanding of astroplasma physics. I thank Prof. Horton for giving me the deep insight of confinement plasma physics and helpful suggestions for developing my research. I also need to thank Dr. Wen-Chien Chou for teaching me how to survive in the Institute for Fusion Studies, how to modify simulation codes, and for many enjoyable discussions. Lastly, I must thank my fellow graduate students, especially Sergey Cheshkov, Edmund Yu, and Ping Zhu for their support in discussing physics-related and non-physics-related subjects.

This work is supported by NSF grant ATM 98-15809, and the US Department of Energy under contract W-7405-ENG-48.

STRUCTURE FORMATION THROUGH MAGNETOHYDRODYNAMICAL INSTABILITIES IN PROTOPLANETARY AND ACCRETION DISKS

Publication No. _____

Koichi Noguchi, Ph.D.
The University of Texas at Austin, 2001

Supervisor: Toshiki Tajima

Structure formation in various astronomical systems through magnetohydrodynamical(MHD) instabilities has been investigated. The effect of magnetic field enhancement in sheared flows is studied as the eigenmode problem in a non-self-adjoint system, and new mathematical and physical aspects of the instability are shown. The mechanism for the faster structure formation in a protoplanetary disk with MHD instabilities is suggested with linear analysis and simulation. Experiments to simulate the plasmas of protoplanetary and active galactic nuclei are also suggested. The coupling of magnetic field enhancement and magnetic buoyancy has been studied and mode coupling of two instabilities are shown.

The stability of nonaxisymmetric perturbations in a differentially rotating astrophysical accretion disk is analyzed by fully incorporating the properties of shear flows. The magnetorotational instability has been investigated as the most promising instability to explain anomalous angular momentum transfer

in accretion disks, and the existence of discrete unstable eigenmode holds a key to resolve this problem.

The apparent narrow window of the age difference of the Sun and the Earth is one of the most difficult problems in the planetary formation theory. The magnetorotational, Parker, and kinematic dynamo instabilities under the presence of magnetic fields in the protoplanetary disk can greatly facilitate the formation of density structures that may provide seeds of protoplanetesimals prior to the onset of the gravitational Jeans instability. The individual effects of these instabilities have been studied over decades, but the combination effects of these instabilities in the protoplanetary formation have not been investigated yet. Such a seeding process may explain the age difference of the Sun and the Earth, as well as other outstanding planetary formation puzzles, which can not be explained by the conventional planetary formation theory, in the planetary genesis. These puzzles are further compounded by the recent discoveries of extrasolar planets and a new insight into the equation of state of dense matter by gas-laser gun experiments.

The unstable eigenmodes with complex and pure imaginary eigenvalues without any artificial disk edge boundaries is shown to be discrete. The nonlocal behavior of eigenmodes in the vicinity of Alfvén singularities at $\omega_D = \pm\omega_A$ is investigated mathematically and physically, where ω_D is the Doppler-shifted wave frequency and $\omega_A = k_{||} v_A$ is the Alfvén frequency. The spectrum of discrete eigenmodes and the dependence of the growth rate on magnetic field and wave number are calculated over a wide range of variables. Exponentially

growing modes may be present even in a region where the local dispersion relation theory claims to have stable eigenvalues. The velocity field created by an eigenmode is obtained, which may explain the anomalous angular momentum transport in the nonlinear stage of this stability.

The effects of the Parker, magnetorotational(Balbus-Hawley), and kinematic dynamo instabilities are evaluated by comparing the properties of these instabilities in protoplanetary disks. The mass spectra of aggregated density structures are calculated by the above mechanism in the radial direction for axisymmetric MHD torus equilibrium and power-law density profile models. The mass spectrum of density aggregates due to the magnetorotational instability may describe the origin of giant planets away from the central star such as Jupiter. Local three-dimensional MHD simulation indicates that the coupling of the Parker and magnetorotational instabilities creates spiral arms and gas blobs in the accretion disk, reinforcing the theory and model. Such a mechanism for the early structure formation for planets may be tested in a laboratory. The recent progress in experiments involving shear flows in rotating tokamak and laser plasmas may become a key element to advance in nonlinear studies. The schematics of protoplanetary and active galactic nuclei disk simulation experiments are suggested based on the growth rate ratio analysis.

The coupling of the magnetorotational and the Parker instabilities is studied here by three-dimensional MHD simulations. The coupling of these instabilities is analyzed linearly, and preliminary results are shown. Due to the coupling of the magnetorotational and the Parker instabilities via magnetic

field, resonant frequencies are coupled. The linear analysis shows that resonances occur not only at Alfvén frequency, but also other frequencies which are coupled with the Brunt-Väisälä frequency.

Table of Contents

Chapter 1

Introductory Outlines

At least 99% by mass of the universe is filled with plasma. More importantly, most of such plasmas are magnetized in which collective interaction plays a crucial role. Such interaction may facilitate or accelerate the evolutionary process of astrophysical objects [1]. One of the most energetic phenomena observed in the universe(i.e. jets ejected from nuclei of active galaxies and quasars) originates from the gravitational energy release in the accretion of outlying mass by central massive objects. Understanding the dynamic behavior of magnetized plasma holds a key to understanding accretion and formation of astronomical objects. The astrophysical question on the formation of jets, galaxies, stars and planets is hinged to such complex disk dynamics. The crucial point of this astrophysical problem is that of collective plasma physics phenomena, which enables the obtaining of a physical understanding of accretion, instabilities and transport processes. How does interstellar cloud lose the angular momentum necessary to accrete to a black hole? Without an efficient removal mechanism of the angular momentum, the gravitational force of a central star or black hole is not sufficient to cause accretion of gravitationally bound gas, since the gas stops its inward fall to the central massive object when the gravitational force in the radial direction is balanced by the centrifugal force of the gas. The tur-

bulent plasma physical process of anomalous transport of angular momentum in the accretion disk is instrumental in understanding the accretion process.

For example, take the problem of planetary genesis. The Sun was born some 4.5 Gyr ago and the Earth(and other planets in our Solar system, it is believed) was also born approximately 4.5 Gyr ago. We may ask why the Earth was created so quickly after the Sun's formation(immediately after the Solar formation, in the astronomical time scale). Can plasma physical processes be used to resolve this puzzle in the rapid formation of planets by accelerating the formation and evolution of protoplanetary structure?

In order to investigate this possibility, we lay a ground framework of the stability of the protoplanetary(and, in fact, general) disk plasma. We recognize that the presence of magnetic fields in such a disk plays a fundamental role in determining their transport properties. The development of such a theory has been hampered, however, by the difficulty of establishing an adequate mathematical frame work to handle the dynamics of sheared flow systems. In this dissertation, three instabilities destabilized by magnetic fields in a disk have been investigated as a key to describing the accretion and planetary formation mechanism. Chapter 2 discusses the stability of nonaxisymmetric perturbations in differentially rotating astrophysical accretion disks. In Chapter 3, planetary formation in a protoplanetary disk has been investigated by linear and nonlinear simulations. Chapter 4 then discusses the stability in accretion disks by including the gravitational effect from the central object of disks.

The outline of the dissertation is as follows. Each chapter is self-contained with respect to the analysis.

Chapter 2: Robustly Unstable Eigenmodes of the Magnetorotational Instability in Accretion Disks

The magnetorotational instability in an accretion disk is studied via linear stability analysis. Unstable nonaxisymmetric eigenmodes in accretion disk are found to be discrete, and the mechanism of anomalous angular momentum transfer via this robust instability in an accretion disk is explained physically and mathematically.

The existence of the anomalous angular momentum transfer is suggested by fitting the theoretical and observed durations of the quiescent and bursting phase of dwarf novae [2]. The most promising instability is the magnetorotational instability, initially discussed by Velikhov [3] and Chandrasekhar [4], and Balbus & Hawley [5] pointed out the importance of this instability in accretion disks. The frame work of global nonaxisymmetric eigenmode analysis of the magnetorotational instability has been done [6], and the eigenmodes they found are examined again to show these eigenmodes are discrete with infinite boundary conditions.

In Chapter 2, the mathematical and physical properties of global nonaxisymmetric eigenmodes of the magnetorotational instability is examined, and eigenmode discreteness is demonstrated using a highly accurate shooting method. The symmetry structure of eigenmodes in the complex-frequency plane and the velocity field is identified. The study of the growth rate on magnetic field strength and wave number determines the maximum growth rate, and reveals merging and splitting of the eigenmodes. The physical and

mathematical characteristics of the eigenmodes at Alfvén resonance points is examined to show energy conversion from kinematic energy to magnetic field energy and vice versa, which is used to postulate a key aspect for anomalous angular momentum transfer in accretion disks.

Robustly unstable discrete eigenmodes present at various radii may overlap with each other, creating a mesoscale radial structures in an accretion disk. This overlapping of local eigenmodes occurs at any radius, making the entire accretion disk turbulent, accelerating the momentum transfer. This overlapping of local modes to form semiglobal eigenmodes is mathematically similar to the global drift wave problem in tokamaks. The importance of the effect was showing by global simulation [7].

Chapter 3: Structure Formation through Magnetohydrodynamical Instabilities in Protoplanetary Disks

The structure formation in protoplanetary disks without self-gravitation is discussed, and the applicability of such shear-flow structure to laboratory plasmas is examined. The structure formation of massive accretion disks, and protoplanetary disks has been discussed with hydrodynamical instabilities [8–13]. Three-dimensional simulations of protoplanetary disks (e.g., [14, 15]) suggest the importance of MHD instabilities, and independent effects of MHD instabilities have been investigated: magnetorotational instability [1,3–5], Parker instability [16, 17], kinematic dynamo [18–21]. Here another possible mechanism is suggested for the protoplanetary formation with the combination of three MHD instabilities. In this chapter, the evolution of a protoplanetary

disk is shown by comparing the growth rate ratios of three MHD instabilities, the magnetorotational, Parker and kinematic dynamo. The Parker instability extracts magnetic field energy from a disk [17], while the others enhance magnetic field energy [1, 3, 4]. Because magnetic field enhancement compensates the magnetic field energy extraction from a disk, the couplings of the Parker and two other instabilities are critical to the study of structure formation. It is found that in the early stage(weakly magnetized) of disk evolution, the magnetorotational instability dominates in the outer($r > 1$AU) region, while the Parker instability is dominant in the inner($r < 1$AU) region. In a later(moderately magnetized) stage, the three instabilities compete with each other, creating complex disk structures.

Based on the linear analysis of growth rate ratios, radial mass spectra are estimated, assuming two different density profiles. The spectrum with a potential density profile [22] has a maximum at some radius in a disk, indicating the global mass accretion in the radial direction by the magnetorotational instability. This dense region can accrete gas further by self-gravitation, and large mass planets, such as Jupiter, may be created in this dense region. Three dimensional local box simulation agrees the results of linear analysis, showing spiral and blob structures in an accretion disk due to the magnetorotational and Parker instabilities.

Even though it is important to measure magnetic viscosity in a protoplanetary disk, direct observational measurement of magnetic viscosity is not easy since the strength of magnetic field in protoplanetary disks is weak($1 \sim 10$ Gauss). The applicability of shear-flow structure to a laboratory created plasma is thus important for measuring the magnetic viscosity experimentally. Exper-

imental simulations of planetary disk plasma issued in a plasma confined in a tokamak or a transiently formed laser created plasma are considered, and the applicability is discussed in terms of the growth rate ratios of the magnetorotational, Parker, and kinematic dynamos. Critical issues for applications to such laboratory plasmas are addressed.

Chapter 4: The Coupling of the Magnetorotational and Parker Instabilities

As I will show in Chapter 3, the coupling of the magnetorotational and Parker instabilities is one of the most critical issues of the structure formation in accretion disks. It is clear that these two instabilities are coupled, since the magnetic field is enhanced by the magnetorotational instability, while the magnetic field energy is continuously extracted from a disk by the magnetic buoyancy(the Parker instability). Three-dimensional MHD simulations(e.g., [14,15]) indicated the importance of the coupling of these instabilities, but this coupling effect has investigated only by solving the initial value problem [23,24]. In this work, the wave equation of eigenmodes, and the coupling is discussed by analyzing singular points of the wave equation. The dispersion relation indicates that the presence of the Alfvén continuum of the magnetorotational instability is maintained even under the influence of the Parker instability, while the Brunt-Väisälä frequency [26] couples with the Alfvén frequency, creating two different continua.

Chapter 2

Robustly Unstable Eigenmodes of the Magnetorotational Instability in Accretion Disks

2.1 Anomalous Angular Momentum Transfer in Accretion Disks

Over the last several years, the presence of magnetic fields in a differentially rotating plasma has become a key ingredient in the consideration of a mechanism of accretion disk turbulence and its associated large anomalous angular momentum transport inside the disk. Various hydrodynamical models without magnetic fields have been investigated to explain this anomalous viscosity: convective turbulence [25, 27], global hydrodynamic shear flow instability [28–30], hydromagnetic turbulence [31–36], and external factors, such as the gravitational field of a companion star [37,38]. However, several investigations [39–41] suggest that the convective turbulence might actually transport angular momentum inward more effectively than outward, i.e. it slows down the accretion. Another problem for the convective turbulence is that disks might be convectively stable [42]. Although hydrodynamic shear flow instability has been studied extensively as a possible mechanism of generating turbulence, its contribution to the anomalous angular momentum transfer was shown to be

too small. The momentum transfer is parameterized by the viscosity parameter $\alpha = \nu/C_s H$, where ν is the viscosity, C_s is the sound speed, and H is the height of an accretion disk, and its value is estimated to be of the order of 0.1 by fitting the theoretical and observed durations of dwarf novae [2]. The contribution of the hydrodynamic shear flow instability was shown to be only $O(10^{-3})$ in geometrically thin Keplerian disks [43]. The presence of a companion star or massive planet, required for the source of external gravitational field, does not seem to be sufficiently general to take into account for disk accretion in most cases. Thus, all of these hydrodynamical instabilities have problems as a candidate to explain the anomalous angular momentum transfer in accretion disks.

The presence of magnetic fields in a sheared rotating gas cylinder makes the gas unstable against axisymmetric perturbations [3,4]. The presence of this robust instability was re-recognized [5] and confirmed by nonlinear ideal MHD simulations [44, 45]. The normal mode analysis [46] of this local magnetorotational instability showed the existence of unstable axisymmetric eigenmodes. This robust instability has been invoked [47] as a most promising candidate mechanism for the anomalous viscosity puzzle(e.g., [1]).

Even though the observed mean magnetic field of the Galaxy is of the order of μG, global simulations shows that dynamo action driven by the magnetorotational instability amplifies the magnetic energy in $10 \sim 20$ rotational periods in accretion disks [48], which is of the order of 10^4yr for the Solar system, to make $\beta = 8\pi P/B^2$ from 1000 to a quasi-steady state with $\beta \sim 10$. Since the mean temperature of an accretion disk is of the order of 100K, the mean magnetic field in an accretion disk can then be $10^{-3} \sim 1$G for electron

density $n_e = 10^4$ cm^{-3}.

A numerical investigation of nonaxisymmetric magnetorotational modes has been carried out by adopting shearing coordinates(e.g., [49]). Matsumoto & Tajima [6] analyzed nonaxisymmetric nonlocal eigenmodes which are sandwiched by two Alfvén singularities around the corotational point and are insensitive to the disk edge boundaries and grow exponentially in time. These modes are distinct from the modes discussed by Ogilvie & Pringle [50], which are nonaxisymmetric modes contained within cylindrical boundaries and whose properties depend strongly on solid edge boundary conditions.

In this chapter, the discreteness of nonaxisymmetric eigenmodes questioned by Ogilvie & Pringle [50] is examined. The analysis is performed in the frame rotating with the local angular velocity, which is adopted in nonaxisymmetric mode analysis [6,50], since eigenmodes evolve exponentially in time. The resolution of this question is important in the theory of accretion disk. Unless this magnetorotational instability is a robust mode insensitive to the boundary conditions, the long search of candidate mechanisms for anomalous viscosity of accretion disks needs to be continued. The criticism of Ogilvie & Pringle [50] is interesting because it reflects the difficulty and the extreme mathematical and physical subtlety involved in the nature of this mode around the Alfvén singularity. The problem is made challenging by the non-self-adjointness of the differential equation that describes eigenmodes, arising from the presence of shear flows. It is important to investigate such a system mathematically and physically in order to understand the argument by Ogilvie & Pringle and to aptly respond to it. In the end such analysis has been developed: it is found that the magnetorotational unstable eigenmodes are discrete, robust and insensitive

to the boundary conditions, as Matsumoto & Tajima originally thought [6]. As stated in §2.2, the main difference between Ogilvie & Pringle and Matsumoto & Tajima are the boundary conditions. Even though both analysis solved identically for the same MHD equations, Ogilvie & Pringle employed solid inner and outer boundaries in the radial direction, whereas Matsumoto & Tajima [6] employed infinite boundary conditions. The eigenmodes derived by Ogilvie & Pringle show strong dependence on the boundaries which indicates the importance of the proper boundary condition in the radial direction, while Matsumoto & Tajima's eigenmodes are confined radially by the Alfvén singular points and can be exited anywhere in a disk.

In §2.2, the wave equation in a differentially rotating magnetized disk is derived again, based on the analysis of Matsumoto & Tajima [6], and then the basic properties of the wave equation are discussed. It is shown that discrete nonaxisymmetric eigenmodes exist, which are buffeted by a pair of Alfvén singularities where the Doppler-shifted wave frequency equals the Alfvén frequency. The numerical calculation of the eigenmodes with their Alfvén frequency and wave number dependence is discussed in §2.3. The results with the local dispersion relation are compared to show these eigenmodes are discrete. Astrophysical implications and conclusions are discussed in §2.4.

2.2 Analytical Properties of Non-Self-Adjoint Equation near Alfvén Singularity

In this section, the MHD stability of magnetorotational modes in the corotating frame of the fluid is considered. The basic ideal MHD equations in

the frame rotating with angular velocity Ω are

$$\left(\frac{\partial}{\partial t}+(\boldsymbol{v}\cdot\nabla)\right)\boldsymbol{v} = -\frac{1}{\rho}\nabla P+\frac{(\nabla\times\boldsymbol{B})\times\boldsymbol{B}}{4\pi\rho}+\boldsymbol{g} + 2\boldsymbol{v}\times\boldsymbol{\Omega}+(\boldsymbol{\Omega}\times\boldsymbol{r})\times\boldsymbol{\Omega}, \tag{2.1}$$

$$\frac{\partial\boldsymbol{B}}{\partial t}=\nabla\times(\boldsymbol{v}\times\boldsymbol{B}), \tag{2.2}$$

where $\boldsymbol{g}$ is the gravitational acceleration and $\boldsymbol{r}$ is the position vector. Incompressibility is assumed for simplicity,

$$\nabla\cdot\boldsymbol{v}=0. \tag{2.3}$$

Note that the sound resonances are suppressed because of incompressibility. Self-gravity is also ignored, which is not essential for the magnetorotational instability.

The local Cartesian coordinates (x, y, z) in the rotating frame are used where the x-axis is in the radial direction, the y-axis in the azimuthal direction, and the z-axis parallel to $\boldsymbol{\Omega}$. For the radius r_0 from the central object, the local angular velocity is Ω and the shear is $d\Omega/dr = -(3\Omega(r_0)/2)/r_0$ for the Keplerian disk. We introduce the linearly sheared velocity $v_y = -(3\Omega(r_0)/2)x$, where $x = 0$ is the local co-rotating radial position. The curvature effect is ignored$(x, y, z \ll r_0)$ in the local coordinates. The wave equation is derived by linearizing the basic equations around the equilibrium state and seeking solution of the form $\tilde{\phi}(x,t)\exp[\mathrm{i}(k_y y + k_z z)]$. The wavenumbers k_y and k_z are assumed to be $k_y r_0 \gg 1$ and $k_z H \gg 1$, where H is the height of the disk, for justifying the assumption of local Cartesian coordinates. The limit of using local Cartesian coordinates will be discussed in §2.4. In this chapter, an accretion disk is assumed to be uniform in the z direction, and the z component

of gravity g_z is ignored, since it destabilize the disk in z direction via the Parker instability. This assumption is valid for the region near the equatorial plane of the disk. In Chapter 4, more general case will be discussed, including uniform gravity in the z direction. Even though the gravity near the equatorial plane of an accretion disk varies as $g_z = g_{z0}z$ as shown in Chapter 3, adding uniform gravity to the system makes it difficult enough.

In the unperturbed state, the density, pressure and magnetic field are taken to be uniform. The assumption of $v_x = v_z = B_x = 0$ in the unperturbed state yields the unperturbed momentum equation,

$$\boldsymbol{g} + 2\boldsymbol{v}_0 \times \boldsymbol{\Omega} + (\boldsymbol{\Omega} \times \boldsymbol{r}) \times \boldsymbol{\Omega} = 0. \tag{2.4}$$

Note that the unperturbed equation has y component, but all the terms are obviously cancelled with each other about $y = 0$ in the local Cartesian coordinate, which agrees with cylindrical coordinates.

Next, the Laplace transform of the perturbation, $\bar{\phi}(x, \omega)$, is employed,

$$\bar{\phi}(x, \omega) = \int_0^\infty dt \tilde{\phi} e^{\mathrm{i}\omega t}. \tag{2.5}$$

Substitution of the Laplace transformed momentum and induction equations into the continuity equation yields (see [6] and Chapter 4 for details) the initial value equation

$$\begin{aligned} &\frac{d^2\bar{v}_x}{dx^2} + \frac{3\Omega\omega_A^2 k_y}{\omega_D(\omega_D^2 - \omega_A^2)}\frac{d\bar{v}_x}{dx} + \Bigg[-(k_y^2 + k_z^2) \\ &-\frac{9\Omega^2 k_y^2 \omega_A^2}{2\omega_D^2(\omega_D^2 - \omega_A^2)} + \Omega^2 k_z^2 \frac{\omega_D^2 + 3\omega_A^2}{(\omega_D^2 - \omega_A^2)^2}\Bigg]\bar{v}_x = \Gamma(x, \omega), \end{aligned} \tag{2.6}$$

where ω_D is the Doppler-shifted frequency,

$$\omega_D = \omega + \frac{3}{2}\Omega k_y x, \tag{2.7}$$

and ω_A is the Alfvén frequency,

$$\omega_A^2 = \frac{(\boldsymbol{k}\cdot\boldsymbol{B})^2}{4\pi\rho} = k_\parallel^2 v_A^2, \tag{2.8}$$

where $k_\parallel^2 = k_y^2 + k_z^2$. The initial conditions of magnetic and velocity fields enter through the source function $\Gamma(x,\omega)$.

The wave equation is derived by expressing the homogeneous part of Eq. (2.6) in terms of the normalized radial coordinate

$$\xi = \frac{3\Omega k_y}{2\omega_A}x = \frac{x}{\Delta x} \tag{2.9}$$

as

$$\begin{aligned}\frac{d^2\bar{v}_x}{d\xi^2} + \frac{2\omega_A^3}{\omega_D(\omega_D^2-\omega_A^2)}\frac{d\bar{v}_x}{d\xi} + \Bigg[-\frac{4}{9}\left(1+\frac{1}{q}\right)\left(\frac{\omega_A}{\Omega}\right)^2 \\ -\frac{2\omega_A^4}{\omega_D^2(\omega_D^2-\omega_A^2)} + \frac{4}{9}\frac{\omega_A^2}{q}\frac{\omega_D^2+3\omega_A^2}{(\omega_D^2-\omega_A^2)^2}\Bigg]\bar{v}_x \\ \equiv D(\omega,\xi)\bar{v}_x = 0,\end{aligned} \tag{2.10}$$

where the ratio of the squares of the azimuthal and vertical wave number is defined as

$$q = \frac{k_y^2}{k_z^2}, \tag{2.11}$$

and Δx is the normalization length in the z direction. The differential equation (2.10) have three singularities, two of which located at $\omega_D = \pm\omega_A$, which are called the Alfvén singular points, and the other at $\omega_D = 0$, called the corotational point. The normalization length Δx can be estimated in terms of q,

$$\Delta x = \frac{2v_A}{3\Omega}\sqrt{\frac{1+q}{q}} = \sqrt{\frac{1+q}{q}}\times 10^9 \sim 10^{13}\mathrm{cm} = \sqrt{\frac{1+q}{q}}\times 10^{-4} \sim 1\mathrm{AU}, \tag{2.12}$$

where $B = 1\mathrm{G}$, $n = 10^4\mathrm{cm}^3$, and $\Omega = 10^-9\mathrm{cm}^{-1}$ is used. The range of Δx, which also determines the length between the Alfvén singular points, is much smaller than the size of the disk unless the perturbation is nearly poloidal($q \ll 1$). Note that Eq. (2.10) is identical to the wave equation of Couette flow between concentric cylinders [4], if the curvature effect is included.

Unstable eigenmodes may exist when the solution satisfies the boundary condition

$$\lim_{|\xi|\to\infty} \bar{v}_x = 0 \tag{2.13}$$

in the upper half of the complex ω-plane reference. This boundary condition makes these eigenmodes distinct from the modes found by Ogilvie & Pringle [50], which are confined in rigid cylindrical boundaries and strongly dependent on the boundary condition. Their problem set up follows the traditional problem of couette flow between concentric cylinder rather than the free boundaries of the infinite domain of astrophysics. In order to have an overall angular momentum transport across the entire disk, it is imperative to have unstable modes within the disk, not just on the boundaries of the disk. To investigate the interior of the accretion disk, eigenmodes should not depend on the edge boundary conditions. The eigenmodes which arise from finite boundaries may contribute to the angular momentum only near the "edge" of the disk. This mode found by Matsumoto and Tajima [6], which is not affected by the edge, grows whenever the eigenfunction is located between two Doppler-shifted Alfvén points. Since the positions of those points are determined in co-rotating frame, the origin of the frame can be anywhere in the disk if the normalization length Δx is smaller than the size of the disk. The boundary condition then assures that the momentum transport resulted from the super-

position of the growing eigenmodes which can occur throughout the accretion disk.

The proper boundary condition interior of the disk can be easily examined by inspecting the asymptotic form of the basic differential equation (2.6) of the system. This indicates that the leading radial dependence of Eq. (2.6) leads to the exponential form $v_x \propto e^{\pm k_x x}$. This mathematics is, of course, most reasonable and physical as well, because the wave energy is provided from one of the two Alfvén singular layer to the mode, whose energy is dissipated again at(or near) the other Alfv/'en singular layer.

Since the wave equation (2.10) is not self-adjoint due to the existence of the flow shear, the square of the eigenvalue ω^2 is not guaranteed to be real, which any self-adjoint system always satisfies. The fact that the eigenvalue is not pure real or imaginary but in general complex prevents us from applying the Strum-Liouville theory to this system. Note that if $k_y = 0$, Eq. (2.6) is reduced to self-adjoint,

$$\frac{d^2\bar{v}_x}{dx^2} + k_z^2\left[-1 + \Omega^2\frac{\omega^2 + 3\omega_A^2}{(\omega^2 - \omega_A^2)^2}\right]\bar{v}_x = 0, \tag{2.14}$$

and its stable eigenvalue constitutes the Alfvén continuum. The analysis of this mode has been done by Chandrasekhar [4]. The stable MHD Alfvén wave continuum consists of singular modes at every singular point $\omega = \omega_A$. The kinetic theory corrections to the MHD Alfvén wave continuum modes is well known [51, 52]. Now k_y is assumed to be $k_y \neq 0$.

It is found that the eigenmodes possess certain symmetry properties, which originate from the character of the differential operator and radial symmetry. The differential operator $D(\omega, \xi)$ is invariant under the operation $(\omega, \xi) \rightarrow$

$(-\omega^*, -\xi)$ because of radial symmetry, where ϕ^* is the complex conjugate of ϕ. Note that the operation $\xi \to -\xi$ is the same as changing the direction of the rotation $\Omega \to -\Omega$. This is a local mirror(reflection) symmetry. Taking conjugate of Eq. (2.10) and changing $-\xi$ to ξ yields

$$D(\omega, \xi)\bar{v}_x(\omega, \xi) = D(-\omega^*, -\xi)\bar{v}_x^*(-\omega^*, -\xi) = 0. \tag{2.15}$$

Thus, if ω is an unstable eigenvalue of Eq. (2.10), $-\omega^*$ is another unstable eigenvalue whose eigenfunction $\bar{v}_x^*(-\omega^*, -\xi)$ satisfies the relation (2.15). Especially, when ω is pure imaginary, i.e., $-\omega^* = \omega$, the real part of eigenfunction is symmetric and the imaginary part antisymmetric with respect to $\xi = 0$,

$$\bar{v}_x^*(\omega, -\xi) = \bar{v}_x(\omega, \xi). \tag{2.16}$$

These properties of the particular non-self-adjoint operator being considered indicates that this system has complex eigenvalues in general, which differs from an ideal MHD self-adjoint system, and one unstable eigenvalue has another unstable companion. This symmetry of non-self-adjoint system and the comparison between self-adjoint and non-self-adjoint eigenvalues in complex-ω plane is shown in Fig. 2.1.

Next, I look for the solution of the wave equation (2.10). The boundary conditions for these ideal MHD modes we are interested in are that the eigenmode resides and is differentiable around the corotational point and sandwiched by a pair of the Alfvén singularities, and decays toward $\xi \to \pm\infty$. Note that these physical boundary conditions preclude the usual Kelvin-Helmholtz(K-H) instability eigenmodes [53, 54]. The boundary conditions generic to the K-H mode is to match the dissipative structure at the corotational point. The

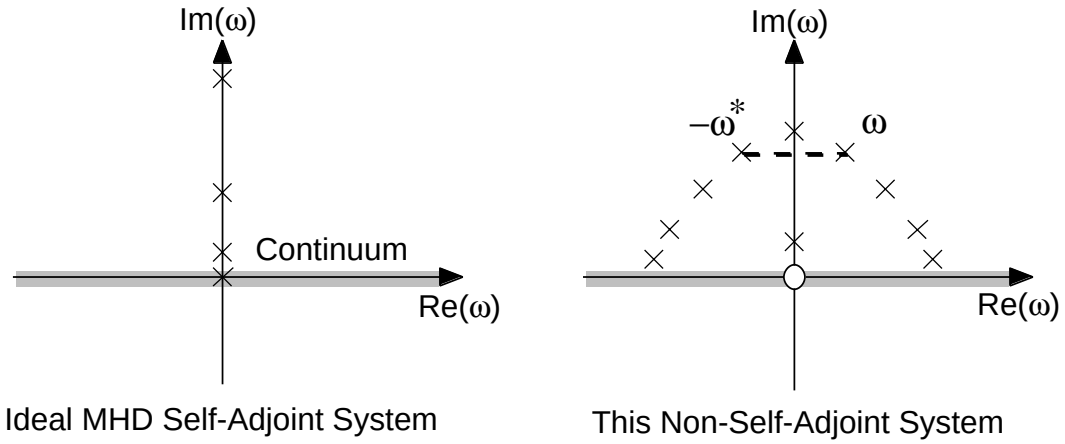

Figure 2.1: Symmetry of a nonself-adjoint system and the comparison between self-adjoint and nonself-adjoint eigenvalues in complex-ω plane. Discrete modes are denoted by crosses. The eigenvalue of the self-adjoint operator should be purely real or imaginary, and the eigenfunctions are predictable by Strum-Liouville theory. However, there is no such restriction for the eigenvalue of the nonself-adjoint operator, and ω and $-\omega^*$ make a pair of unstable solutions, indicated by a dashed line in the figure.

properties of these eigenmodes may be investigated by analyzing the solution around the spatial coordinates of interest by using the Frobenius expansion [55], in particular around the Alfvén singular points. It is of particular significance to examine analytical properties of the Frobenius expression around the Alfvén singularities in order to examine the question raised by Ogilvie & Pringle [50] against the eigenmodes obtained by Matsumoto & Tajima [6]. An appropriate, compatible numerical method for these eigenmodes is, therefore, the shooting method that starts from an exponentially decaying functional form at $\xi = \pm\infty$ and shoots toward the corotational point ξ_c, where two sides of the function should smoothly (differentiably) match.(This will be closely examined in the next section.)

The velocity $\bar{v_x}$ in Eq. (2.10) is expanded using,

$$\bar{v}_x(\xi, s) = \sum_{n=0}^{\infty} a_{n\pm}(\xi - \xi_{A\pm})^{n+s} \tag{2.17}$$

in the vicinity of the Alfvén singularities $\omega_D = \pm\omega_A$ or $\xi = \xi_{A\pm}$, where $\xi_{A\pm}$ is defined by

$$\begin{aligned} \xi_{A\pm} &= \pm 1 - \frac{\omega}{\omega_A} \\ &= \pm 1 - \omega_r' - \mathrm{i}\omega_i', \end{aligned} \tag{2.18}$$

and $\omega_r'(\omega_i')$ is the real(imaginary) part of ω/ω_A. Assuming $\omega_i' \ll 1$ and applying the Frobenius method in the vicinity of the regular singular points $\xi = \mathrm{Re}(\xi_{A\pm})$, the indicial equation for the exponent s for Eq. (2.10) is given by

$$s^2 + \frac{\omega_i'(\omega_i' \pm 3\mathrm{i})}{2 \mp 3\mathrm{i}\omega_i' - \omega_i'^2} s + \frac{4}{9q}\left[\frac{4 \mp 2\mathrm{i}\omega_i' - \omega_i'^2}{(2 \mp \mathrm{i}\omega_i')^2}\right] = 0. \tag{2.19}$$

Note that the eigenfunction is irregular and oscillates indefinitely at $\xi = \xi_{A\pm}$ whenever s has imaginary component, provided $\mathrm{Re}(s)$ is nonpositive integer,

$$\bar{v}_x(\xi, s) = (\xi - \xi_{A\pm})^{\mathrm{Re}(s_\pm)} \exp\left[\mathrm{Im}(s_\pm) \log|\xi - \xi_{A\pm}|\right]. \tag{2.20}$$

The singular points are on the real axis if and only if the eigenvalue ω is real. In general, the indices are given by

$$\begin{aligned} s_\pm = \frac{\omega_i'(\omega_i' + 3\mathrm{i})}{2(2 - \mathrm{i}\omega_i')(1 - \mathrm{i}\omega_i')} \times \Bigg[&-1 \\ &\pm \sqrt{1 - \frac{16}{9q}\frac{(4 - 2\mathrm{i}\omega_i' - \omega_i'^2)(1 - \mathrm{i}\omega_i')^2}{\omega_i'^2(\omega_i' + 3\mathrm{i})^2}} \Bigg], \end{aligned} \tag{2.21}$$

for $\xi = \xi_{A+}$, and

$$\begin{aligned} s_\pm = \frac{\omega_i'(\omega_i' - 3\mathrm{i})}{2(2 + \mathrm{i}\omega_i')(1 + \mathrm{i}\omega_i')} \times \Bigg[&-1 \\ &\pm \sqrt{1 - \frac{16}{9q}\frac{(4 + 2\mathrm{i}\omega_i' - \omega_i'^2)(1 + \mathrm{i}\omega_i')^2}{\omega_i'^2(\omega_i' - 3\mathrm{i})^2}} \Bigg], \end{aligned} \tag{2.22}$$

for $\xi = \xi_{A-}$. Since s is not integer, being typically an irrational complex number, the solution is not analytic at the Alfvén singular points.

Now, some special cases are investigated. First, when the eigenvalue is pure real, i.e., $\omega_i' = 0$, the indices are purely imaginary,

$$s = \pm \frac{2}{3\sqrt{q}}\mathrm{i}, \tag{2.23}$$

the eigenfunction oscillates indefinitely towards the singular point. As the eigenmodes oscillate indefinitely around the Alfvén singularity, it is found that the eigenvalue becomes continuous in this pure real case to form the Alfvén continuum. Note that the boundary condition in this case becomes special in that we need to shoot outward from $\xi = \xi_c$. Here ξ_c is the corotational point where $\omega_D = 0$ or $\xi_c = -\omega/\omega_A$. We can no longer shoot from the outer boundaries to the region between two Alfvén singular points without introducing dissipation in the vicinity of the Alfvén resonance points.

At Alfvén resonance points, nonlinear energy transfer occurs due to the kinetic Alfvén wave dissipation by wave particle interactions [51, 56]. The spatial length of the dissipation is determined by introducing finite ion Lamor radius, and the boundary conditions at the boundaries between the resonance and wave regions allow us to connect the inner and outer solutions.

Second, when $\omega_i' \ll 1$, which is similar to the first case but now the singular points are not on the real axis, the solutions are

$$s_\pm = \pm \left[\frac{2}{3\sqrt{q}}\mathrm{i} - \frac{3}{32}\sqrt{q}\omega_i' \right], \tag{2.24}$$

for $\xi = \xi_{A+}$, and

$$s_\pm = \pm \left[\frac{2}{3\sqrt{q}}\mathrm{i} + \frac{3}{32}\sqrt{q}\omega_i' \right], \tag{2.25}$$

for $\xi = \xi_{A-}$, whose solution oscillates limited times in the vicinity of the singular points on the real axis, but not indefinitely, and the solution is regular on the real axis.

Third, when the perturbation is nearly toroidal ($k_y \gg k_z, q \gg 1$), as in the accretion disks far from their source, the eigenvalue is complex. In this case, square term in s is expanded to the order of $1/q$, which yields

$$s_\pm = \frac{\omega_i'(\omega_i'+3\mathrm{i})}{2(2-\mathrm{i}\omega_i')(1-\mathrm{i}\omega_i')} \times \left[-1 \pm \left(1 - \frac{8}{9q} \frac{(4-2\mathrm{i}\omega_i' - \omega_i'^2)(1-\mathrm{i}\omega_i')^2}{\omega_i'^2(\omega_i'+3\mathrm{i})^2} \right) \right], \tag{2.26}$$

for $\xi = \xi_{A+}$, and

$$s_\pm = \frac{\omega_i'(\omega_i'-3\mathrm{i})}{2(2+\mathrm{i}\omega_i')(1+\mathrm{i}\omega_i')} \times \left[-1 \pm \left(1 - \frac{8}{9q} \frac{(4+2\mathrm{i}\omega_i' - \omega_i'^2)(1+\mathrm{i}\omega_i')^2}{\omega_i'^2(\omega_i'-3\mathrm{i})^2} \right) \right], \tag{2.27}$$

for $\xi = \xi_{A-}$. When the perturbation is pure toroidal, the second term in the square brackets in Eqs. (2.26) and (2.27) vanishes and s is given by

$$s = 0, \quad -\frac{\omega_i'(\omega_i'+3\mathrm{i})}{(2-\mathrm{i}\omega_i')(1-\mathrm{i}\omega_i')}, \tag{2.28}$$

for $\xi = \xi_{A+}$, and

$$s = 0, \quad -\frac{\omega_i'(\omega_i'-3\mathrm{i})}{(2+\mathrm{i}\omega_i')(1+\mathrm{i}\omega_i')}, \tag{2.29}$$

for $\xi = \xi_{A-}$. The eigenfunction corresponding to $s = 0$ is regular, and the latter one diverges logarithmically at the singular point, when ω is real. Finally, when the perturbation is nearly poloidal($k_y \ll k_z, q \ll 1$), as may occur in accretion disks close to their source, s is

$$s_\pm = \pm \frac{2\mathrm{i}}{3\sqrt{q}} \frac{\sqrt{4-2\mathrm{i}\omega_i' - \omega_i'^2}}{2-\mathrm{i}\omega_i'}, \tag{2.30}$$

for $\xi = \xi_{A+}$, and

$$s_{\pm} = \pm \frac{2\mathrm{i}}{3\sqrt{q}} \frac{\sqrt{4 + 2\mathrm{i}\omega_i' - \omega_i'^2}}{2 + \mathrm{i}\omega_i'}, \tag{2.31}$$

for $\xi = \xi_{A-}$, which reduces to the roots of the first case when the eigenvalue is pure real.

The exponent s at the corotation point $\omega_D = 0$ (or $\xi_c = -\omega/\omega_A$) is given by

$$s = \frac{1}{2(\omega_i'^2 - 1)} \left[\omega_i'^2 - 3 \pm \sqrt{\omega_i'^4 - 14\omega_i'^2 + 17} \right]. \tag{2.32}$$

When $\omega_i'^2 \geq 7 + 4\sqrt{2}$, the eigenvalue is regular at the corotation point, since both indices are real and positive. When $0 \leq \omega_i'^2 < 1$, indices are still real, and one of them is positive. This is the solution that is consistent with the matching condition at $\xi = 0$ of the shooting method discussed in §3. When $1 < \omega_i'^2 \leq 7+4\sqrt{2}$, the corotation point is singular since two indices are real and negative in the region $1 < \omega_i'^2 \leq 7-4\sqrt{2}$, and complex in the region $7-4\sqrt{2} < \omega_i'^2 < 7 + 4\sqrt{2}$. When $\omega_i'^2 = 1$, the eigenfunction has irregular singularity at the corotation point. Again, even though the eigenfunction is irregular at the corotation point, the physical eigenmodes on the real ξ-axis is regular. Moreover, since all the coefficients of the differential equation (2.10) are real at the corotation point even when the eigenvalue is complex, the eigenfunction should be real at $\xi = \xi_c$.

Although irregular in the vicinity of the Alfvén singularities or the corotation point in most cases, eigenfunctions are not irregular in the physical sense unless the singularities are on the real axis. Instead, the oscillatory behavior and amplitude of the eigenfunction around the Alfvén singularities directly reflects the physical eigenfunction behavior on the real ξ-axis, especially if ω_i'

is small, i.e., the Alfvén frequency is larger than the imaginary part of an eigenfrequency, $\omega_A \gg \omega_i$.

When the eigenvalue ω and the index s are both complex, the eigenfunction oscillates indefinitely in the vicinity of the singularity due to the imaginary component of the index s(see Eq. [2.20]). In this case, the physical eigenfunction on the real ξ-axis also oscillates very rapidly in the vicinity of the point which is the projection of the complex singular point to the real ξ-axis, but the physical eigenfunction oscillates only finite times because the projected point is not a singular point.

When the real component of s is negative, the eigenfunction diverges at the singularity(Eq. [2.20]). The amplitude of the physical eigenfunction on the real ξ-axis is large at the projected singular point on the real ξ-axis. However, since the projected point is not a singular point, the eigenfunction does not diverge at this point. It is also clear that the eigenvalue is regular even if the singular point is a branch point, since the branch cut of the eigenvalue can be chosen without crossing the real ξ-axis.

If the eigenvalue is real, the singularities are on the real ξ-axis and eigenfunction is irregular in the physical sense. Pure real eigenvalue cases will be discussed in §2.3.

2.3 Robustly Unstable Magnetorotational Eigenmodes

The eigenvalues of the wave equation (2.10) are calculated numerically by the shooting method with the boundary condition discussed in §2.2. Since Eq. (2.10) may have three singularities(corotation point and two Alfvén res-

onances), complex initial value is chosen to avoid Alfvén singularities on real axis, and integrate("shoot") Eq. (2.10) on the real ξ-axis from the left and right asymptotic boundaries(which are far removed from any of the particular singular points) to the corotation point, where their value and first derivative of the eigenmode are to be matched. If they are not matched, the eigenvalue ω' is changed appropriately until it will be matched. This iterative method is generally called the "shooting method" for eigenvalue problems. Spatial steps of the integration are smaller in the vicinity of the point where the Alfvén point is projected on the real ξ-axis than other regions, in case the eigenvalue is almost real but still complex. By using the Newton method to decrease errors of a trial function [57], higher accuracy and faster convergence than the previous shooting codes is obtained. The error in the trial function is measured by the squares of the function itself and the first derivative of it at the matching point. This allows me to search for subtle singular and regular eigenfunctions over a wide range of parameter values.

In order to satisfy the boundary condition (2.13), $\bar{v}_x'/\bar{v}_x = k_\pm$ is imposed at the numerical boundaries $\xi = \pm 10$ (corresponding to the artificial infinity), where $k_\pm$ are the negative and positive solutions of the quadratic equation given by inserting the functional form $\bar{v}_x = \exp(k_\pm x)$ into Eq. (2.10). In the calculations below, on the numerical boundaries $\xi = \pm 10$, the leading term of Eq. (2.6) is always the first term of the coefficient of $\bar{v}_x$, which is of the order of 1, and other terms are of the order of 0.01 or lower, which justify to use the exponential asymptotic solution on the numerical boundaries. The assumption for the boundary condition is valid as far as these estimations are valid.

Figure 2.2 shows examples of eigenfunctions $\bar{v}_x$ obtained by this shoot-

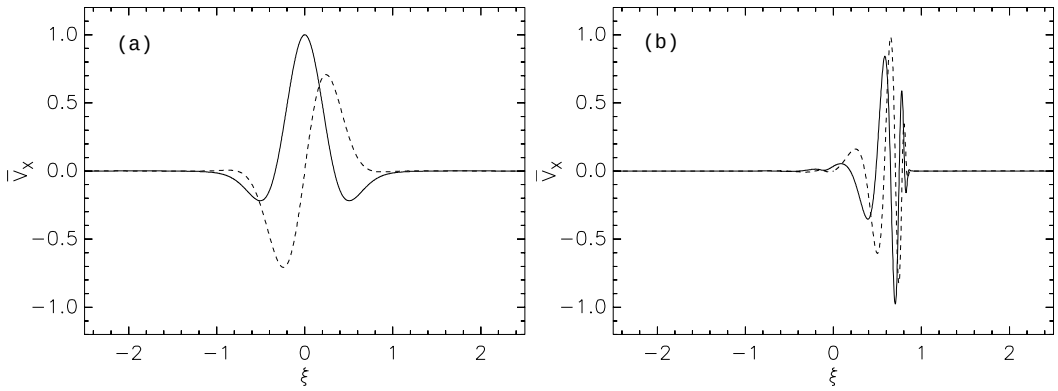

Figure 2.2: Examples of the eigenfunctions of the nonaxisymmetric magnetorotational instability in a Keplerian disk. *Solid curve,* real part of eigenfunction; *dashed curve,* imaginary part of eigenfunction. The model parameters are $\omega_A = 0.1\Omega$ and $q = 0.01$. (a) Fundamental pure imaginary mode(eigenvalue is $\omega = 0.00785\Omega\mathrm{i}$); (b) Complex mode[eigenvalue is $\omega = (0.00109 + 0.00039\mathrm{i})\Omega$]. The eigenfunctions are sandwiched by two Alfvén singularities $\xi = \pm 1 - \omega/\omega_A$ which on the scale of the figure are indistinguishable from $\xi = \pm 1$ and the corotational point is indistinguishable from $\xi = 0$.

ing code when $\omega_A = 0.1\Omega$ and $q = 0.01$. The solid and dashed curves represent the real and imaginary parts of the eigenfunction respectively. Fig. 2.2a is for the fundamental pure imaginary eigenvalue and Fig. 2.2b is for the complex eigenvalue. Since the eigenvalue of Fig. 2.2a is pure imaginary, the real part of the eigenfunction is symmetric and the imaginary part antisymmetric with respect to $\xi = 0$, which is consistent with Eq. (2.16). Fig. 2.2b is the eigenfunction with a complex eigenvalue, which makes a pair with the eigenvalue $-\omega^*$ whose eigenfunction is derived from the relation (2.15). These eigenfunctions are confined between two Alfvén singularities located at $\xi = \xi_{A\pm} \sim \pm 1$, and they are real at $\xi = \xi_c$.

Figure 2.3 shows the distribution of eigenvalues in the upper complex ω-plane when $\omega_A/\Omega = 0.01$ and $q = 0.01$. It shows only the eigenvalues in the region $\mathrm{Re}(\omega) \geq 0$, and all the complex eigenvalues have a paired eigenvalue

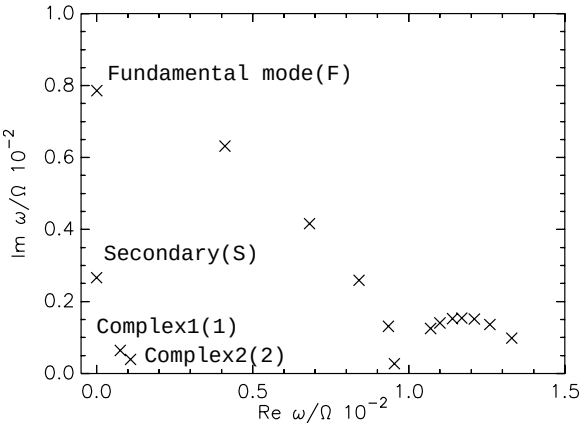

Figure 2.3: Distribution of unstable eigenvalues of the magnetorotational instability in the upper complex ω-plane when $\omega_A = 0.1\Omega$ and $q = 0.01$. Eigenvalues with $\mathrm{Re}(\omega) < 0$ are shown, and all the complex eigenvalues have a paired unstable eigenvalue $-\omega^*$ in the region $\mathrm{Re}(\omega) < 0$. There exist only two pure imaginary eigenmodes and many complex eigenmodes, which are not allowed to exist in self-adjoint system.

$-\omega^*$ in the region $\mathrm{Re}(\omega) < 0$. It is obvious that this non-self-adjoint system has complex eigenvalues, which does not appear in an ideal MHD self-adjoint system (see Fig. 2.1). There are only two pure imaginary eigenvalues, which will be shown to merge by changing ω_A and q. Complex eigenvalues, which Matsumoto & Tajima [6] did not find, exist and have smaller imaginary part and grow slower in time than the fundamental eigenmode.

Figure 2.4 shows the dependence of unstable eigenvalues on ω_A when $q = 0.01$. The solid(dashed) curves show the imaginary(real) part of the eigenvalues. When ω_A is small, there exist two purely growing modes, which merge at $\omega_A \sim 0.66\Omega$ and form complex eigenvalues. These modes were found in Matsumoto & Tajima [6] and the qualitative properties of this mode are about the same as found in Matsumoto & Tajima. However, the merging point is slightly greater than the earlier value and, more significantly, the growth rate does not decay

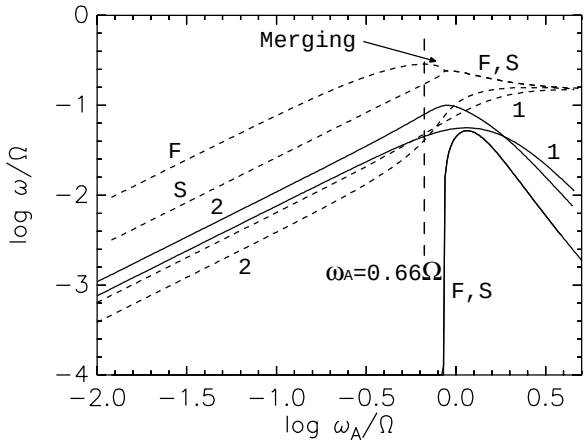

Figure 2.4: The Alfvén frequency ($\omega_A = k_{\|} v_A$) dependence of eigenvalues of magnetorotational instability when $q = 0.01$. The dashed curves and solid curves show the growth rate Im(ω) and the real frequency Re(ω), respectively. The fundamental(F) and secondary(S) pure imaginary eigenmodes and two complex modes(1, 2) are shown, which correspond to the eigenmodes labeled F, S, 1 and 2 in Fig. 2.3, respectively, when $\omega_A/\Omega = 0.01$. Two pure imaginary eigenvalues merge at $\omega_A \sim 0.66\Omega$ to form complex eigenvalues. The growth rate of all four eigenvalues saturates to $\omega \sim 0.15\Omega$i with increasing ω_A.

significantly, even beyond $\omega_A = 1.584\Omega$, where it was calculated to vanish in Matsumoto & Tajima [6]. The fundamental mode acquires its maximum growth rate just before it merges with another(secondary) pure imaginary mode. In addition, two new complex modes are found, called modes 1 and 2 for brevity. These complex eigenmodes are labeled as 1 and 2 in Fig. 2.4, and the growth rate of all these modes saturate to $\omega \sim 0.15\Omega$i, the same saturation value for the fundamental mode with increasing ω_A.

Figure 2.5 shows the dependence of eigenvalues on $q = k_y^2/k_z^2$, which is the dimensionless measure of the direction of propagation in yz-plane, when $\omega_A = 0.01\Omega$ (Fig. 2.5a) and 0.66Ω (Fig. 2.5b). The fundamental(F) and secondary(S) pure imaginary modes and two complex modes(1, 2) are shown in Fig. 2.5, which correspond to the eigenmodes in Fig. 2.4, when $q = 0.01$.

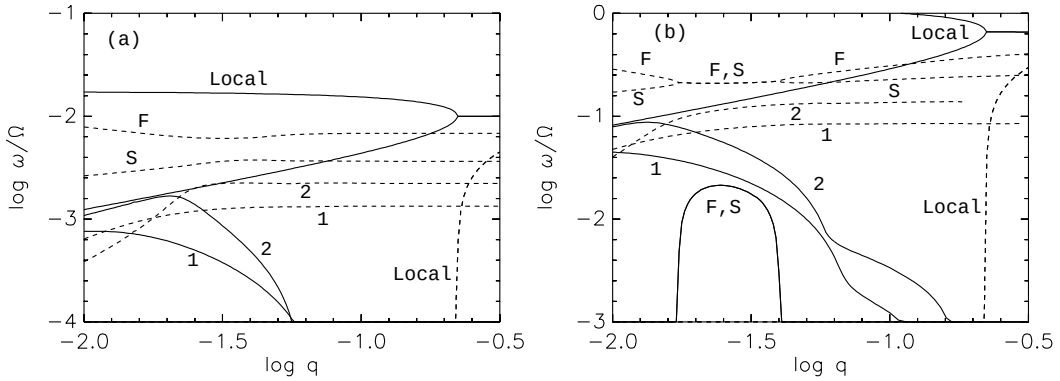

Figure 2.5: The $q(=k_y^2/k_z^2)$ dependence of eigenvalues of magnetorotational instability. The dashed curves and solid curves show the growth rate Im(ω) and Re (ω), respectively. The fundamental(F) and secondary(S) pure imaginary modes and two complex modes(1, 2) are shown, which correspond to the eigenmodes labeled F, S, 1 and 2 in Fig. 2.4 when $q = 0.01$. Eigenvalues calculated from local mode analysis are also shown. (a) $\omega_A = 0.01\Omega$. Two pure imaginary eigenmodes(F, S) are always distinct, and the complex eigenmodes(1, 2) become pure imaginary, whose growth rate saturates, with increasing q. (b) $\omega_A = 0.66\Omega$. Two pure imaginary eigenvalues(F, S) merge at $\log_{10} q \sim -1.8$ to form complex eigenvalue, and split again to become imaginary at $\log_{10} q \sim -1.4$. The complex eigenmodes(1, 2) becomes pure imaginary with increasing q, and the growth rate saturates. In both cases, local modes are stable even in a region where nonlocal modes are unstable.

Eigenvalues calculated from local analysis are also shown in Fig. 2.5, which will be discussed later. Two pure imaginary modes are always distinct when $\omega_A = 0.01\Omega$ (two upper modes in Fig. 2.5a). However, when $\omega_A = 0.66\Omega$, these two modes merge and become complex at $\log_{10} q \sim -1.8$ and split to become pure imaginary again at $\log_{10} q \sim 1.4$. The eigenvalues of the other two complex modes become pure imaginary when q exceeds a certain value ($\log q = -1.25$ for $\omega_A = 0.01\Omega$, $\log q = -0.75$ for $\omega_A = 0.66\Omega$), and the growth rate for those modes saturates with increasing q.

Next, the nonlocal eigenfunction results with the local(Fourier) dispersion relation are compared. By replacing d/dx in Eq. (2.6) with a con-

stant ik_x around $x = 0$ and assuming that the unperturbed magnetic field is toroidal($B_x = B_z = 0$), the local solution in the regime

$$|\omega| \sim \omega_A \ll \omega_e \equiv \sqrt{\Omega^2 k_z^2/(k_x^2 + k_y^2 + k_z^2)}$$

is [6]

$$\omega^2 = \frac{3}{2}\left[1 - \frac{3}{2}q \pm \frac{3}{2}\sqrt{(q-2)(q-\frac{2}{9})}\right]\omega_A^2, \tag{2.33}$$

where ω_e is the epicyclic frequency. This local dispersion relation (2.33) shows that pure real eigenmodes appear in the region $q < \frac{2}{9}$, pure imaginary eigenmodes in $q > 2$, and complex in $\frac{2}{9} < q < 2$. However, when q is small, i.e., the perturbation is almost parallel to the magnetic field, nonlocal eigenmodes are unstable in both $\omega_A = 0.01\Omega$ and 0.66Ω (see Figs. 2.5a, b), and the growth rate of each mode does not have strong dependence on q. It is concluded that replacing $\partial/\partial x$ by a single wave number k_x is invalid for these modes since such eigenmodes oscillate very rapidly in the vicinity of the Alfvén points in a pronounced fashion(see Fig. 2.2b). In other words, the spatial variation of the wave number in the radial direction is essential for the modal analysis of the magnetorotational instability. Radial dependency of the wavelength also prevents us from applying the WKB method to this model. The WKB method requires the wavelength of the eigenmodes L_e is smaller than the shear scale length $L_s(L_e/L_s \ll 1)$, which may be satisfied around the corotational and Alfvén singularities, but the wavelength is comparable to the shear scale length in other regions($L_e/L_s \simeq 1$).

To show that these eigenmodes are discrete, the existence of the Alfvén continuum on the real ω-axis is shown first. The wave equation (2.10) has a solution for any real ω for which $\omega_D^2 = \omega_A^2$ for some x. It follows that the

spectrum of this mode is continuous, and the Alfvén continuum extends to the all real ω by choosing some k_y and k_z, which is different from the model chosen by Ogilvie & Pringle [50] in which the Alfvén continuum is restricted by the boundary condition. The eigenmodes with the pure imaginary eigenvalue that shown above are obviously not in this class. Note that the eigenvalue is pure imaginary only on the corotational point $\xi = \xi_c$, and local frame with other radii see Doppler-shifted complex eigenfrequency.

When $\boldsymbol{B} = 0$, the Kelvin-Helmholtz modes can be derived, which are stable in accretion disks. In this limit, Eq. (2.6) reduces to

$$\frac{d^2\bar{v}_x}{dx^2} + \left[-(k_y^2 + k_z^2) + \frac{\Omega^2 k_z^2}{\omega_D^2}\right]\bar{v}_x = 0, \tag{2.34}$$

and when $k_z = 0$, it has a simple solution $\bar{v}_x = \exp[-k_y|x|]$, which satisfies the boundary condition (2.13). The first derivative of this class of solutions is discontinuous at $x = 0$, which vanishes with introducing dissipation. The Kelvin-Helmholtz instability also has continuous eigenvalues, but this class of solutions is eliminated in the calculation because of the matching condition of the shooting method, which requires the eigenfunction and its first derivative to be continuous. In contrast, the continuum modes are delta function-like solutions. Eigenvalues are searched by choosing initial trial eigenvalues in the region $0 < \omega_r/\omega_A < 1$ and $0 < \omega_i/\omega_A < 1$. These initial trial values are iterated to minimize an error measure and found to converge to one of the eigenvalues in Fig. 2.3. All the eigenmodes subject to the boundary condition (2.13) are concluded to be discrete.

In Fig. 2.6, another eigenmode is shown, whose eigenvalue gradually becomes real with increasing q, when $\omega_A = 0.66\Omega$. However, when the eigenvalue

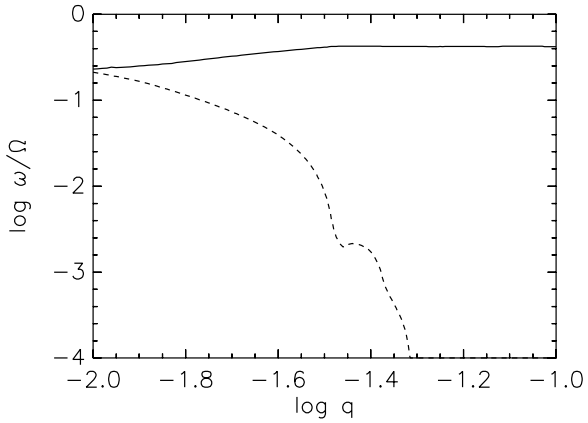

Figure 2.6: The example of a complex eigenmode that becomes pure real value with increasing q when $\omega_A = 0.66\Omega$. The dashed curve and solid curve show the growth rate $\mathrm{Im}(\omega)$ and the real frequency $\mathrm{Re}(\omega)$, respectively. The eigenvalue is complex when q is small, which becomes real with increasing ω_A. The grid size Δq in this figure is $\log(\Delta q) = 0.02$.

is real, it have been already shown that the index of the eigenfunction s is pure imaginary in the vicinity of the Alfvén singularities [Eq. (2.23)] and that the eigenfunction has the form

$$\bar{v}_x = \exp\left[\mathrm{i}s \log|\xi - \xi_{A\pm}|\right], \tag{2.35}$$

from Eq. (2.20). Such eigenfunctions have the local radial wavenumber strongly increasing as $k_x(\xi) = s/(\xi - \xi_{A\pm})$ with the number of oscillations(in phase) increasing to $s \log \xi_{min}$. Here ξ_{min} is limited by the ion radius [56]. This indicates that the function in the inner region $\xi_{A-} < \xi < \xi_{A+}$ and outer region $\xi < \xi_{A-}, \xi < \xi_{A+}$ is discontinuous at the Alfvén singularities. Thus the boundary condition for the continua cannot be that of shooting from the outside $|\xi| = \infty$ toward the inside, but it should be shot from inside toward the singularities.

Figure 2.7 shows an example of eigenfunction in the inner region when

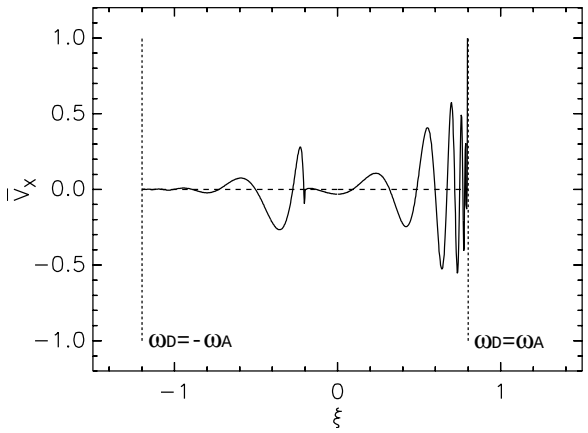

Figure 2.7: The mode with a pure real frequency that has the Alfvén singularities at $\omega_D = \pm\omega_A$, where the mode energy evanesces. The eigenfunction oscillates indefinitely towards $\omega_D = \omega_A$, and also towards $\omega_D = -\omega_A$ with small amplitude. Here $\xi = 0$ defines the radial position that is in co-rotating with the wave of frequency ω in a global internal reference frame.

$\omega_A = 0.01\Omega$, $\omega = 0.002\Omega$ and $q = 0.01$(see Eq. (2.23) and arguments for detail of this mode). However, the eigenmode in Fig. 2.6 is continuous even at the Alfvén singular points, since the integration by a finite spatial step brings in an effective dissipation, which is not the case for the pure real eigenvalue. Instead, the eigenmode becomes continuous because of the numerical dissipation. Although this numerical eigenfunction is different from the theoretical eigenfunction beyond the passage of the singularity, the fact of continua remains the same for two different reasons. It should be pointed out that in real physical situation there always exists a dissipation(collisional or turbulent) even for a nearly ideal MHD system. The dissipation prevents the eigenmode from blowing up on the Alfvén singular points, keeping the energy of the eigenmode finite. Introducing the finite ion Lamor radius also prevents the eigenmodes from blowing up, transferring wave energy to kinematic energy. The numerical dissipation affects this eigenmode in the same manner mathematically as the

physical dissipation does, by passing oscillations through the singularity barrier and averaging oscillation in a finite spatial step. Thus the numerically obtained eigenmode, though different from theoretical Alfvén continua, may be regarded as realistic.

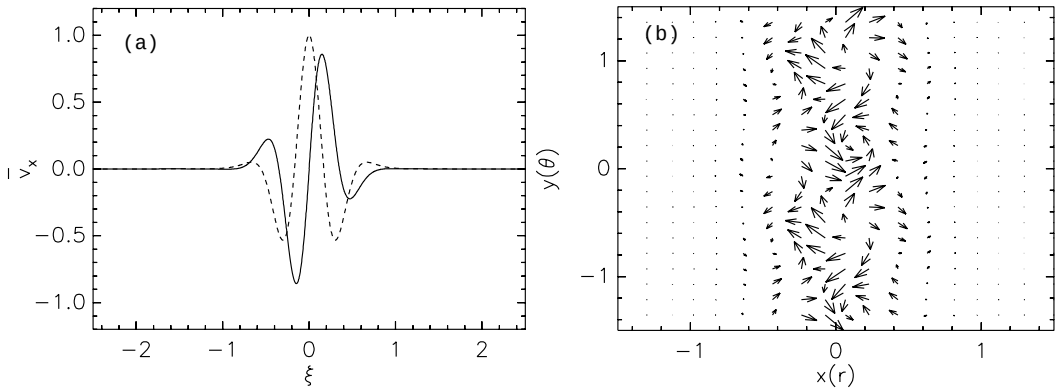

Figure 2.8: An example of $\bar{v}_y$ calculated from the fundamental pure imaginary mode (Fig. 2a) and the velocity field in xy-plane by the fundamental mode. The solid curve and dashed curves show the real and imaginary part of $\bar{v}_y$, respectively. (a) $\bar{v}_y$ is almost out of phase with respect to $\bar{v}_x$. (b) Velocity field is created in xy-plane by the fundamental mode. Vortices are created between two Alfvén singularities, and they will overlap with other eigenmodes excited at various x-positions to expand the unstable region.

Finally, the physical behavior of the eigenmodes in accretion disks is described. The expression of $\bar{v}_y$ in terms of $\bar{v}_x$ is derived from the equation of continuity(2.3),

$$\bar{v}_y = \frac{\mathrm{i}}{1+q}\left[\frac{q}{k_z}\frac{\partial}{\partial\xi} - \frac{\omega_D\Omega}{2(\omega_D^2-\omega_A^2)}\left(3\frac{\omega_A^2}{\omega_D^2}+1\right)\right]\bar{v}_x. \tag{2.36}$$

Figure 2.8a shows $\bar{v}_y$ calculated from the fundamental pure imaginary mode (Fig. 2.2a) and the velocity field created in the xy-plane by the fundamental eigenmode is shown in Fig. 2.8b. The eigenfunction of $\bar{v}_y$ is also trapped between two Alfvén singularities. Since both $\bar{v}_x$ and $\bar{v}_y$ are almost out of phase with each other, the velocity field created by the fundamental eigenmode

consists of vortices in xy-plane which are the seeds of nonlinear instability [6]. Note that since the frame rotating with angular velocity Ω is used, there is no unique origin x in the xy-plane. Thus such unstable eigenmodes excited at various x-positions will overlap with each other to expand the unstable region in the x-direction.

2.4 Summary of Chapter 2

The unstable nonaxisymmetric magnetorotational instability eigenmodes in accretion disks has been examined by mathematical and physical analysis to show the discreteness of these modes in infinite plasma. Since the exponentially decaying boundary condition was assumed (Eq. [2.13]) for the radial component of velocity, these modes are almost(to within exponential small variation) independent of the global radial boundary conditions since $k_{\pm}\xi_b \gg 1$, where $k_{\pm} = \bar{v}_x'/\bar{v}_x$ and ξ_b is the value of ξ at the artificial boundary. This robust instability occurs without any unrealistic disk edge boundary condition in infinite linear shear flow. However, for nearly axisymmetric perturbations($k_y \ll k_{\|}$), the eigenmode have a large radial scalelength, and then global radial boundary condition will effect the modes. The density profile $\rho(r)$ and geometrical effects become important in this case. The scalelength of a single eigenmode in the x direction, Δx, is determined by the local strength of magnetic field divided by the Keplerian shear flow rate(B/A), the direction and amplitude of the wave number, and the magnitude of the angular velocity (see Eqs. [2.7] and [2.8]), since the eigenfunction is buffeted by the Alfvén singular points $\omega_D = \pm\omega_A$. If the magnetic field is pure toroidal, $\Delta x = 2\omega_A/3\Omega k_y = 2v_A/3\Omega \simeq (2/3)(v_A/C_s)H$, where C_s is the sound speed and

$H = C_s/\Omega$ is the thickness of the disk. When $v_A \ll C_s$, the mode is localized in the radial direction with the scalelength smaller than the thickness of the disk. If the magnetic field has vertical component, Δx is proportional to $k_\parallel/k_y$ [6]. Typical scale length is $\Delta x = 10^{-4} \sim 1$ AU [Eq. (2.12)]. In both cases, the infinite boundary condition is sufficient if the scalelength of the eigenmode is smaller than H. The curvature of the magnetic field is also small if $\Delta x \ll H$.

The results of the growth rate analysis of unstable modes agrees with that of Matsumoto & Tajima [6] in the region $\omega_A \leq \Omega$. I also found complex eigenvalues with smaller growth rates than the fundamental pure imaginary eigenmode. When ω_A is larger than Ω, two pure imaginary eigenmodes merge, the results of which is the same as found in Matsumoto & Tajima. However, it is found that the decrease of the growth rate saturates with increasing ω_A, which indicates that the accretion disk is unstable even if the Alfvén frequency is comparable to the angular velocity, a case of strong magnetic fields.

The comparison of the nonlocal and local dispersion relations demonstrates where and how the local Fourier mode approximation [5] fails to be accurate for this nonaxisymmetric instability. The wave number dependence of the eigenvalue shows that the nonlocal modes are unstable even in the region $q = k_y^2/k_z^2 \ll 1$, where the local dispersion relation has only a stable solution. Furthermore, two pure imaginary eigenvalues have been found to merge to be complex and to split into two pure imaginary again with increasing q(almost pure toroidal perturbation) in a region where the solutions of the local dispersion relation are purely real. Overall, as Fig. 2.5 indicates, the discrepancy of the local theory from more precise nonlocal theory amounts to not just a quantitative change (as Matsumoto & Tajima suggested [6]) but a qualitative

change in the physical picture. This change is due to the strong radial propagation induced by the co-rotational singularities. The local mirror symmetry is shown to be an important constraint on the spectrum.

The mathematical and physical views of a non-self-adjoint MHD fluid system with radial symmetry has been investigated. In astrophysics, nonself-adjointness always appears whenever there is a shear flow. A pair of complex eigenvalues ω and $-\omega^*$, which an ideal MHD self-adjoint system does not have, relate to each other in this model, since the model is symmetric with respect to the radial direction.

Although this model of the nonaxisymmetric mode is linear in Cartesian coordinates and ignore the effect of diffusion, analysis in Section 2.3 suggests how the eigenmode grows to enter a nonlinear stage, and how it explains momentum transport in accretion disks by analogy with the global drift wave in a tokamak [7]. Since there is no particular sense in the radial direction in Cartesian coordinates, there exists no specific calibration of momentum transport in the linear stage. The eigenmodes can be excited, however, between any pair of Alfvén singularities in the radial direction with the typical wavelength Δx, and create vortices in the disk plane (the xy-plane), as shown in Fig. 2.8b. The eigenmode with the fundamental eigenvalue dominates in time for a given radial co-rotation point because of the largest growth rate. For another (arbitrary) co-rotation point, the same applies. These eigenmodes may overlap with each other to form larger vortices by vortex merging process. In this stage, the nonlinear effect gives rise to anomalous magnetic viscosity that underlies the momentum transport needed to explain astrophysical disks.

Matsumoto & Tajima [6] demonstrated non-linear evolution of the eigen-

mode by three-dimensional MHD simulation with the shearing-box model. The overlap of eigenmodes excited at various x-positions was shown. They also calculated the magnetic viscosity parameter

$$\alpha_B = -\frac{\langle \delta B_x \delta B_y \rangle}{4\pi\rho C_s^2} < \frac{\langle \delta B^2 \rangle}{4\pi\rho C_s^2} \simeq \frac{k_\parallel^2 v_A^2}{k_\perp C_s^2} \tag{2.37}$$

where the notation $\langle \delta B_x \delta B_y \rangle$ denotes the spatial average of $\delta B_x \delta B_y$. They found that when the poloidal field is dominant, the magnetic viscosity is $\alpha_B \sim O(0.1)$, which corresponds to the inferred α_B in dwarf novae during the bursting phase [2].

Here it is concluded that the magnetorotational unstable nonaxisymmetric eigenmodes in accretion disks are discrete, and that the robust mode in magnetized accretion disks is of the magnetorotational origin. This mode should be dominant in nonlinear theory and the presented linear analysis supports the results from the three-dimensional simulation in Matsumoto & Tajima, which gives a quantitative model for anomalous momentum transport in accretion disks.

As discussed in §2.3, the parameter search in the complex-ω plane shows the existence of discrete unstable eigenmodes in a uniform magnetic field, which clearly shows the argument of Ogilvie & Pringle [50] is incorrect. Not only their theoretical argument of non-existence of eigenmodes with uniform magnetic field has been shown to be incorrect [63], but also they might search eigenvalues numerically in incorrect way. They claimed that they searched the same parameter region as Matsumoto & Tajima and found no eigenmode. However, since they derived wave equation in local Cartesian coordinate from cylindrical coordinate and took the rigid boundaries away to the infinity, the resulted wave

equation is different from what Matsumoto & Tajima derived.

Our results do not exclude the existence of Ogilvie & Pringle's mode associated with their rather ad hoc radial boundary conditions of rigid walls at r_1 and r_2. However, our eigenmode is robustly unstable almost everywhere in a accretion disk, while their mode can be excited only in the vicinity of disk edge boundaries, contributing substantial momentum transfer around the disk edges.

Chapter 3

Structure Formation through Magnetohydrodynamical Instabilities in Protoplanetary Disks

3.1 Three Fundamental Questions from Observation

Many believe that the evolution of the Solar System and other like systems with newly discovered planets [58] is critically dependent on the formation of the central star and its disk(protoplanetary disk). Yet, it is puzzling that the age of the Sun is currently estimated to be within a few percent of that of the Earth of 4.5 Gyr, indicating that the formation of the Earth must have been very swift right after the formation of the Sun [59–62]. Despite decades of research, the mechanism of planetary formation has yet to be fully understood [8–13]. The self-gravitation of gas in an accretion disk is too slow to trigger the creation of planets. The presence of magnetic field in the plasma of the protoplanetary disk may play a greater role than has been acknowledged so far. In fact, Tajima and Shibata [1] find in general that the presence of magnetic fields in an astrophysical object such as the galactic disk tends to accelerate the evolution of the astrophysical object by facilitating the faster transport of angular momentum of the system, via the formation of jets, loops, clumps, and turbulence. Perhaps this general tendency of accelerated evolu-

tion facilitated by the presence of magnetic fields is once again an important factor in understanding the formation of planets. The presence of magnetic fields introduces more energetic robust instabilities [48]. These instabilities are an agent to create large density perturbations strong enough to set in the Jeans instability. The role of magnetic fields should arise in an early stage of the accretion disk evolution. In Chapter 2, accretion disks have been shown to be unstable to the magnetorotational instability [3–6, 63], which speeds up the evolution of accretion disks by transporting angular momentum outward and making the disks turbulent. This instability enhances magnetic field in the disk, providing a prominent role of the magnetohydrodynamical(MHD) instabilities, while hydrodynamical instabilities in accretion disks have failed to provide an effective transport mechanism at low levels of ionization(see Chapter 2 and corresponding refs). At very low ionization levels the geostrophic and baroclinic turbulence of the rotating neutral gas dominates, which were shown to be slow for the structure formation of protoplanetary disks [25–27, 31–36]. Plasma physics contributes to the resolution of the question of the planetary formation in its contemporary context. This also implies that perhaps for the first time in history of planetary genesis research(which started with Kant's disk theory) a laboratory simulation experiment of the primordial planetary disk plasma may be conducted to assist theoretical understanding of this important question.

There are three major questions arising from observation which the previous theoretical view of planetary formation can not answer. First, fifty or so giant extrasolar planets have been discovered recently [58,64,65]. The mass and distance from the host star of most of these extrasolar planets are far different

from those of the solar system's. Thus the theory of the conventional Solar system's genesis [8–13] does not apply. Computer simulations suggest that once the core of such a giant planet is formed, the core accretes the gas around it in a few million years [13], if the density clumps can contact to each other before they are tidally disrupted. Complex gravitational interactions with other young planets may make those small planets bounced out of their solar systems or plunge into their parent suns, which can be avoided by the self-gravitational mechanism [66]. However, the creation of the core itself of a giant planet from gas cannot be explained by the self-gravitation without episodic mass accretion onto the disk [67] or an existence of companion star [68].

Second, the gas-laser gun experiments of dense hydrogen [69–71] sheds a new understanding of the metallic hydrogen and the equation of state of hydrogen in the Jupiter. The basic idea of these experiments is compressing liquid hydrogen by gas gun to pressures from 0.9 to 1.8 Mbar, reducing the energy gap between the filled valence-electron band and the unfilled conduction-electron band down to the thermal energy. Conductivity measurements shows the metallization of hydrogen occurs at ~ 1.4 Mbar, and the resistivity falls almost four orders of magnitude [69]. Conventional theory suggests that the Jupiter and Saturn formed by the core accretion mechanism [8,9], which is a two-step process. First, solid core of a $\sim 10 M_{\oplus}$ created in ~ 0.5Myr. Second, as this core grows, a growing atmosphere of nebular gas collapses onto the protoplanet's envelope in several million years or more [72]. The solid core at the center of the Jupiter is required to maintain the observed density [10]. However, the equation of state of hydrogen from the metallic hydrogen experiments imply that the solid core of Jupiter may not exist, or at least it is much smaller than

expected [69]. Since the conventional convection theory of large mass planets relies on the gravitational accretion of gas by the solid core, the first stage accumulation of planetesimals did not occur, and needs longer time to form such planets. Once again, there should be more robust mechanism rather than self-gravitation to quickly evolve giant planets in their early phase.

Third, it is enigmatic that the estimated time scales of the Sun's and the Earth's ages are so nearly comparable [59–62,73,74]. If only self-gravitation acts to evolve the planetary formation, considering that the Earth was formed subsequent to the solar formation, there is little time for planetary genesis [59–62]. Though how the evolution of our solar system is an unsolved problem, the magnetorotational instability is the most plausible mechanism for the anomalous angular momentum transfer by MHD turbulence in the accretion disk [6, 63], accelerating structure formation in a disk.

In the present chapter new idea is introduced that the MHD instabilities, particularly the magnetorotational(Balbus-Hawley) instability [3,4], the Parker instability [17] and the kinematic dynamo [18], play a crucial role to trigger an early structure formation of protoplanetary disk density perturbations. The physical properties of their structure formation are presented such as the growth times and expected mass spectrum of formal density perturbations, which can lay a foundation for the later prompt evolution of planets.

In Sec. 3.2, the importance of the MHD instabilities in the evolution of protoplanetary disks is discussed. The characteristics of the Parker and magnetorotational instabilities and kinematic dynamo are discussed in Sec. 3.3. The mass spectra in the radial direction are evaluated in Sec. 3.4, and the results of the three-dimensional MHD simulations are shown in Sec. 3.5. Applicability

of the shear-flow induced structure to laboratory plasmas is examined in Sec. 3.6. Section 3.7 applies these results to an observation and theoretical view of accretion disk evolution.

3.2 Magnetohydrodynamic Processes of the Protoplanetary Disk

MHD instabilities are important in the early stage of the protoplanetary evolution for the following reasons.(We show a schematic view of the system in Fig 3.1.)

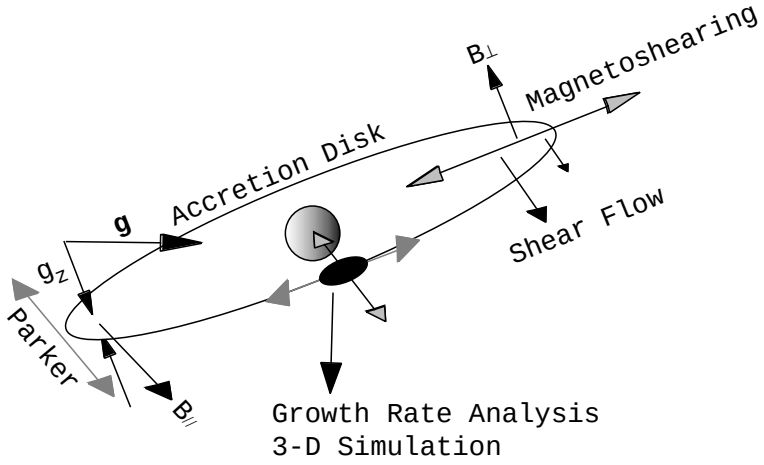

Figure 3.1: A schematic view of MHD instabilities in early stage of the protoplanetary evolution. Shear flow and magnetic field makes an accretion disk unstable to the magnetorotational instability. The disk is also unstable to the Parker instability because of gravity from the central star and magnetic field inside of the disk.

In the inner region of the accretion disk, axial(poloidal) magnetic fields from the central object and azimuthal ones converted from the former and vice versa can be enhanced exponentially in several disk rotations due to the kinematic dynamo [18]. In the outer region, the magnetorotational instability

renders the disk turbulent, which also converts axial and azimuthal components of magnetic field into each other and enhances their strength exponentially in time (see Chapter 2). As the magnetic pressure inside of the disk grows, the disk becomes unstable to the Parker instability because of the magnetic buoyancy. The Parker instability accumulates matter as blobs at the foot points of the magnetic loops on the disk, while it extracts magnetic field energy away from the disk [16]. Once these blobs develop, the Jeans instability sets in to dominate the evolution of protoplanets. All of these processes except for the Jeans instability do not need self-gravitation, accelerating the evolution of planets in the early pre-self-gravitation stage.

The evolution of an accretion disk remains a challenging problem. The main problem arises from the treatment of the flow shear in the accretion disk. Local analysis of shear flows(i.e. the Fourier analysis) fails due to the radial nonuniformity of the accretion disk, which also limits the applicability of the WKB method to this problem as explained in the previous chapter. The nonlocal eigenvalue problem is adopted [6,63].

The other problem is the creation and extraction of magnetic field energy. Three-dimensional simulations showed that the magnetic field in an accretion disk is enhanced due to the magnetorotational instability [15,48], as a result of which buoyancy becomes strong enough to make the disk unstable to the Parker instability. The magnetic field forms loops emanating from inside to outside of the disk because of the Parker instability [1,48]. Since magnetic field is incessantly created from both the magnetorotational instability and kinematic dynamo, this dynamic process occurs recursively, or in other words, is self-sustained. Moreover, the disk remains turbulent due to the magnetorota-

tional instability. Turbulence is essential for the kinematic dynamo [18]. The combination of these instabilities is a complex problem to analyze. In this chapter, these instabilities are compared to estimate which instability is dominant under what conditions.

Some of the processes associated with this structure formation of a plasma with shear flows may be studied in laboratory plasmas such as tokamaks and in laser experiments. Recent experiments show that toroidal shear flows in tokamak creates the radial momentum transport as well as barrier inside of plasma which regulates momentum transfer to the wall [75]. Though the strength of magnetic field and density of plasma are different from the accretion disk case, the configuration of the system and the instabilities which may occur in tokamak experiments can be similar to those of the accretion disk system. Drift wave vortices in the layer corotating with Jupiter toroidal plasma called the Io plasma Torus provides another example [76]. Both the Io plasma torus and the tokamak plasma have $P \ll B^2/8\pi$ in contrast to the accretion disk plasma. Shear flows and magnetic fields make plasma unstable to the magnetorotational instability, and the curvature of magnetic field in the toroidal direction makes plasma Rayleigh-Taylor(Parker) unstable [4]. Thus, the unstable conditions may be experimentally examined in tokamak devices. In experiments trying to simulate supernovae, the surface of target suffers the Rayleigh-Taylor instability [77]. If sheared rotation and magnetic field, essential for the magnetorotational instability, are applied to the target, we may be able to simulate the accretion disk evolution by laser experiments. Parameters are estimated for those cases and discuss if such experiments are plausible.

3.3 The Parker, magnetorotational, and Kinematic Dynamo instabilities

The MHD shear flow instabilities, either the magnetorotational or the dynamo instabilities, play a role of an agent that keeps(or enhances) the presence and strength of the disk magnetic field and its turbulent level [15,48]. These two instabilities, by and large, determine the amount of mass that may be aggregated. The elevated level of magnetic fields in the disk through these instabilities gives rise to the activation of the Parker instability. The nonlinear evolution of the Parker instability is known [1, 16, 78, 79] to produce high density plasma blobs at the feet of the unstable buoyant loop. This nonlinear evolution is in fact a robust mechanism that can yield a significant density structure within a matter of several multiples of the rotating period [48]. Note that this mechanism can be operative well before the self-gravitational Jeans instability becomes effective. These instabilities require a weak, but finite initial poloidal or dipolar magnetic field, which can be created from the magnetic field of Galaxy($\sim 1\mu$G) in several rotational periods [48].

For simplicity, curvature effect is ignored and the local Cartesian coordinates $(x, y, z)$is used in the local co-rotating frame at r_0 at frequency $\Omega(r_0)(x, y, z$ are the radial, azimuthal, and vertical directions). The sheared angular velocity v_y arising from $\Omega(x/r_0) = \Omega(r_0) - 2A(x/r_0)$ is assumed for $x = r - r_0$, where $A = -(rd\Omega/dr)/2$ is Oort's constant(Fig. 3.2).

Under a constant vertical gravity g_z without Coriolis force, the growth rate of the Parker instability γ_P is [17]

$$\gamma_P^2 = \frac{C_s^2}{\beta+2}\left[\sqrt{4\left(1+\frac{1}{\beta}\right)^2\left(k_y^2+\frac{1}{4H^2}\right)^2+2\left(1+\frac{2}{\beta}\right)\left(\frac{1+1/\beta}{H^2}-2k_y^2\right)k_y^2}\right.$$

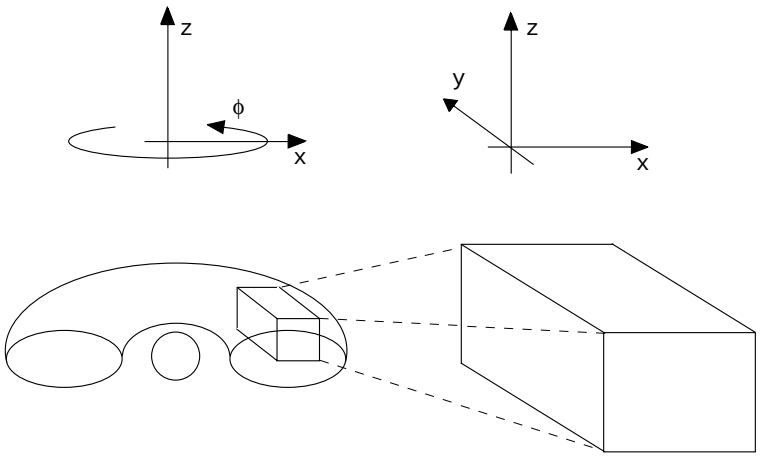

Figure 3.2: Simulation region and the local Cartesian coordinate.

$$-2\left(1+\frac{1}{\beta}\right)\left(k_y^2+\frac{1}{4H^2}\right)\Bigg] \quad (3.1)$$

where H is the vertical scale height of the disk, $C_s = \sqrt{\gamma P/\rho}$ is the sound speed, $\beta = 8\pi P/B^2$, and k_y is the wave number in the azimuthal direction, respectively. The height H depends on g_z by $g_z = (1+1/\beta)C_s^2/H$. It is also assumed that $k_x H \ll 1$ for maximum growth rate, where k_x is the radial component of the wave number. The maximum growth rate is given by

$$\begin{aligned}\gamma_P^2 &= \frac{C_s^2}{H^2}\frac{\left[\sqrt{(\beta+1)^3}+(\beta+1)\left(2\sqrt{\beta^5}+5\sqrt{\beta^3}+2\sqrt{\beta}-2\sqrt{(\beta+1)^5}\right)/2\right]}{\sqrt{\beta^3}(\beta+2)} \\ &= \frac{g_z}{H}\frac{\left[\sqrt{(\beta+1)}+\left(2\sqrt{\beta^5}+5\sqrt{\beta^3}+2\sqrt{\beta}-2\sqrt{(\beta+1)^5}\right)/2\right]}{\sqrt{\beta}(\beta+2)} \end{aligned} \quad (3.2)$$

with

$$k_y^2 = \frac{\beta+1}{4H^2}\left[-(2\beta+3)+\sqrt{(2\beta+3)^2+\frac{3\beta+4}{\beta}}\right] \quad (3.3)$$

When $\beta \geq 1/2$, Eqs. (3.2) and (3.3)can be reduced as $k_y^2 = 3/16H^2$ and [17]

$$\gamma_P^2 = \frac{C_s^2}{8H^2\beta} = \frac{g_z}{8(1+\beta)H}. \quad (3.4)$$

For $\beta \leq 0.1$, $k_y^2 = (2/\sqrt{\beta} - 3)/4H^2$ gives the maximum growth rate

$$\gamma_P^2 = C_s^2 \frac{(2-3\sqrt{\beta})(5\beta/2 - \sqrt{\beta}+1)}{4\beta(\beta+1)(1-\sqrt{\beta})H^2} = \frac{(2-3\sqrt{\beta})(5\beta/2-\sqrt{\beta}+1)}{4(1+\beta)^2(1-\sqrt{\beta})H} g_z. \quad (3.5)$$

The comparison of the full formula (3.1) and the estimated maximum formulae (3.4) and (3.5) is shown in Fig. 3.3.

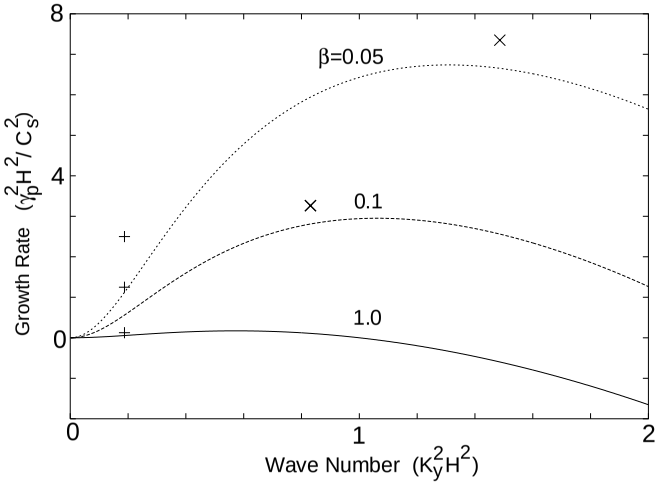

Figure 3.3: The comparison of the full formula (3.1) and the estimated maximum formulae (3.4) and (3.5). The growth rates of the Parker instability for $\beta = 0.01, 0.1, 0.2$ are shown as the function of k_y. The estimated maximum values calculated by formulae (3.4) and (3.5) are also shown.

When the magnetic field is purely toroidal, the maximum growth rate of the magnetorotational instability γ_{mr} can be estimated from the local dispersion relation [6],

$$\begin{aligned} \gamma_{mr}^2 &= \frac{A}{\Omega - A}\omega_A^2 \\ &\propto \frac{A}{\Omega}\omega_A^2 \times 10^{-1} \end{aligned} \quad (3.6)$$

where $\omega_A^2 = (\boldsymbol{k}\cdot\boldsymbol{B})^2/4\pi\rho$ is the Alfvén frequency. For Keplerian disk the O'ort constant is $A = 3\Omega/4$, and $\gamma_{mr}^2 = 3\omega_A^2$ Since global analysis shows that the

growth rate is maximum when $\omega_A/\Omega \sim 1$ [63], the maximum growth rate for the magnetorotational instability is $\gamma_{mr}^2 \sim 0.1A\Omega$. The growth time is several to dozen multiplies of the rotation period of the disk. In formulae (3.1)-(3.6), the ionization is assumed substantial so that the magnetic Reynolds number $R_m = v_A H/\eta$ is sufficiently large to freeze the magnetic field into the plasma motion for times of order $1/\gamma_{mr}$ and $1/\gamma_P$.

The ratio of the squared growth rates is introduced to assess the relative importance of these two processes as

$$\mathcal{R} = \frac{\gamma_{mr}^2}{\gamma_P^2} \simeq A\Omega \frac{(1+\beta)H}{g_z} \times 10^{-1}, \tag{3.7}$$

for $\beta \gg 1$ and

$$\mathcal{R} \simeq A\Omega \frac{0.4(1+\beta)^2(1-\sqrt{\beta})H}{(2-3\sqrt{\beta})(5\beta/2-\sqrt{\beta}+1)g_z}, \tag{3.8}$$

for $\beta \ll 1$. For the protoplanetary disk, $\beta \gg 1$ since magnetic field in a accretion disk is weak to begin with. The vertical gravitational force of the central object can be expressed by the radius r from the center and the height z from the equator of the disk,

$$g_z = \frac{GMz}{(r^2+z^2)^{3/2}}, \tag{3.9}$$

where G is the gravitational constant and M is the mass of the central object. When $r \gg z$, g_z is reduced to GMz/r^3. Since $\Omega = \sqrt{GM/r^3}$ and $A = 3\Omega/4$ for the Keplerian disk, the ratio (3.7) is written as

$$\mathcal{R} = 0.6(1+\beta)\frac{H}{|z|}. \tag{3.10}$$

In this case, the number of Parker e-foldings in one rotation period is

$$2\pi\gamma_P/\Omega = \frac{\pi\beta}{1+\beta}\sqrt{\frac{1}{2\beta}}\frac{\Omega|z|}{C_s}, \tag{3.11}$$

showing the dominance of the Parker instability away from the equatorial plane of the disk. On the surface of an accretion disk($|z| = H$), $\mathcal{R}$ only depends on β. If a protoplanetary disk is not too weakly magnetized($\beta = 10$), $\mathcal{R}$ is of the order of unity. Since the vertical gravity decreases towards the equatorial plane of the disk, $\mathcal{R}$ increases as $|z|$ decreases. However, if it is more strongly magnetized($\beta < 1$), the ratio $\mathcal{R}$ is calculated from Eq. (3.8),

$$\mathcal{R} = \frac{0.3(1+\beta)^2(1-\sqrt{\beta})}{(2-3\sqrt{\beta})(5\beta/2-\sqrt{\beta}+1)}\frac{H}{|z|}. \tag{3.12}$$

Though the magnetization of the disk rarely becomes this high, Eq. (3.12) indicates the dominance of the Parker instability on the surface of the strongly magnetized disks($\mathcal{R} < 1$). Therefore, the magnetorotational instability is dominant in the early stage of the disk evolution($\beta \gg 1$), and the magnetization of the disk increases with time due to the magnetorotational instability. In the later stage($\beta \sim 1$), the Parker instability sets in because of the enhanced magnetic fields, and the Parker instability dominates the evolution of the surface of the disk, whereas the magnetorotational instability still enhances magnetic fields near the equatorial plane($|z| \ll H$). Figure 3.4 shows the time evolution of $\mathcal{R}$ on the disk surface $z = H$ as the function of the magnetic field strength $1/\beta$.

Next, the growth rates of the kinematic dynamo and the Parker instability are compared. The $\alpha\omega$ dynamo is evaluated, which includes the effect from helicity(α effect) and from the differential rotation effect(ω effect). The governing equations of kinematic dynamo are [16]

$$\left(\frac{\partial}{\partial t} - \eta\nabla^2\right) B_y = \frac{dv_y}{dz}\frac{\partial A_y}{\partial x} - v_y\frac{\partial B_y}{\partial y}, \tag{3.13}$$

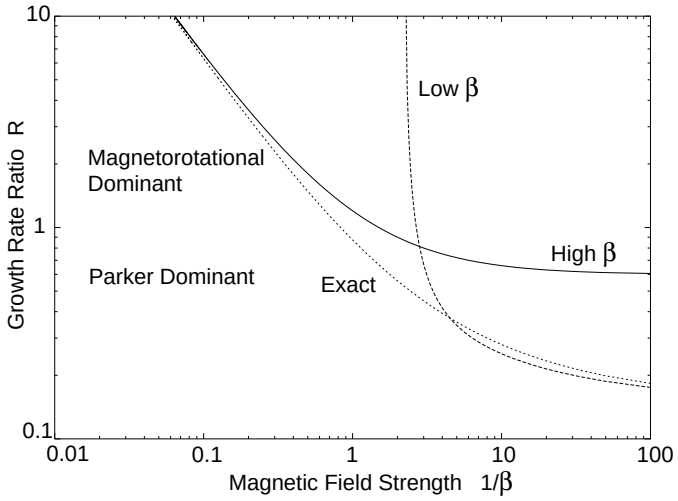

Figure 3.4: The growth rate ratio $\mathcal{R}$ on the disk surface $z = H$ as the function of the magnetic field strength $1/\beta$ using Eq. (3.2). The ratios with reduced formulas [Eqs. (3.10) and (3.12)] are also shown. In the early stage[$1/\beta < 1$, Eq. (3.10)], the magnetorotational instability is dominant($\mathcal{R} > 1$). In the later stage[$1/\beta > 1$, Eq. (3.12)], the Parker instability sets in($\mathcal{R} \sim 1$).

$$\left(\frac{\partial}{\partial t} - \eta\nabla^2\right) A_y = \alpha B_y - v_y \frac{\partial A_y}{\partial y}, \tag{3.14}$$

where α is the mean helicity times the correlation time $\tau_c\langle \boldsymbol{v} \cdot \nabla \times \boldsymbol{v}\rangle$, η is the effective magnetic diffusivity, and A_y is the azimuthal component of vector potential associated with the poloidal magnetic field($\boldsymbol{B}_p = \nabla A_y \times \hat{\boldsymbol{y}}$). The growth rate of the $\alpha\omega$ dynamo is given by [1],

$$\gamma_d = \eta k^2 \left[\mathrm{Re}\left(\sqrt{-\frac{k_y^2 v_y^2}{4\eta^2 k^4} + 2\mathrm{i}N_d} \right) - 1 \right], \tag{3.15}$$

where $k^2 = k_x^2 + k_y^2 + k_z^2$ is the square of the dynamo wave number, and

$$N_d = \frac{\alpha k_z}{2\eta^2 k^4} \frac{dv_y}{dx}, \tag{3.16}$$

is the dynamo number, respectively. The parameter α is of the order of the turbulent velocity $\boldsymbol{v}_z$ in the vertical direction. The base level resistivity set

by electron-neutral collisions is small typically estimated as $\eta_r = 10^6$ cm^2 s^{-1}. However, the turbulent fluid motions produce a large effective resistivity. It is assumed that the turbulent motion in the inner region produces a resistivity $\eta = 10^{16}$ cm^2 s^{-1} [19] for a typical dynamo number for dipole $N_d \sim 600$. Since α can be estimated as $\alpha = \alpha_0(r/r_0)^{-3/2} = v_y(r_0)(r/r_0)^{-3/2} \times 10^{-2}$, N_d depends on r as $N_d = N_d(r_0)(r/r_0)^{-3}$ [19]. The wave number k is estimated by assuming $k_x \simeq k_z \geq k_y$ in eq. (3.16), which yields $k_x H \simeq k_z H = O(10^{-1})$. In this case, the dispersion relation (3.1) which is valid for the case $k_x H \gg 1$, cannot be used, and another expression for $k_x H \ll 1$ is introduced [17],

$$\gamma_P^2 = \frac{C_s^2}{2}\left[\sqrt{\left(1+\frac{2}{\beta}\right)^2\left(k_y^2+\frac{1}{4H^2}\right)^2+\frac{4k_y^2}{\beta}\left(\frac{1+1/\beta}{H^2}-2k_y^2-\frac{1}{2H^2}\right)}\right.$$
$$\left.-\left(1+\frac{2}{\beta}\right)\left(k_y^2+\frac{1}{4H^2}\right)\right]. \quad (3.17)$$

When $\beta \gg 1$, the maximum growth rate arises for $k_y^2 = (\sqrt{2}-1)/4H^2$ and is

$$\gamma_P^2 = \frac{(\sqrt{2}-1)g_z}{(1+\beta)H}, \quad (3.18)$$

while for $\beta \ll 1$, $k_y^2 = (\sqrt{2/\beta}-3)/4H^2$ gives the maximum growth rate

$$\gamma_P^2 = \frac{\sqrt{\beta}\,g_z}{4(1-\sqrt{\beta})(1+\beta)H}. \quad (3.19)$$

Now another growth rate ratio $\mathcal{R}_d$ is introduced for comparing the growth rate of the Parker instability to that of the $\alpha\omega$ dynamo with same wave number k_P,

$$\mathcal{R}_d = \frac{\gamma_d^2}{\gamma_P^2} = \frac{4(\sqrt{2}-1)}{(1+\beta)}\frac{\eta^2 k^4 H}{\Omega^2|z|}\left[\mathrm{Re}\left(\sqrt{-\frac{k_y^2 v_y^2}{4\eta^2 k^4}+2\mathrm{i}N_d}\right)-1\right], \quad (3.20)$$

for $\beta \gg 1$, and

$$\mathcal{R}_d = \frac{\sqrt{\beta}}{(1-\sqrt{\beta})(1+\beta)}\frac{\eta^2 k^4 H}{\Omega^2|z|}\left[\mathrm{Re}\left(\sqrt{-\frac{k_y^2 v_y^2}{4\eta^2 k^4}+2\mathrm{i}N_d}\right)-1\right], \quad (3.21)$$

for $\beta \ll 1$. For the small thick disk case($r \sim 1$AU,$H/r \sim 0.1$) with temperature 100K, $\mathcal{R}_d = O(10^{-1})$ with $\beta = 10$ and $\mathcal{R}_d = O(1)$ with $\beta = 0.1$ on the surface of the disk. Thus, the dynamo effect is weak at the beginning of the protoplanetary evolution($\beta \gg 1$), and magnetic fields created by the dynamo($z \ll H$) cannot be maintained because of the Parker instability. However, in the later stage of the evolution($\beta \ll 1$), the magnetic field is supplied from the central star, and then maintained by the dynamo effect. The Parker instability and the dynamo effect makes the inner region turbulent. Note that the $\alpha\omega$ dynamo generates magnetic field only in the inner region($r = 2 \sim 3$AU) of the protoplanetary disk. Since $\mathcal{R}_d$ is proportional to k^4, small structure due to the $\alpha\omega$ dynamo grows faster than that of the Parker instability even when $\beta \ll 1$. Figure 3.5 shows the time evolution of $\mathcal{R}_d$ on the disk surface $z = H$ as the function of the magnetic field strength $1/\beta$.

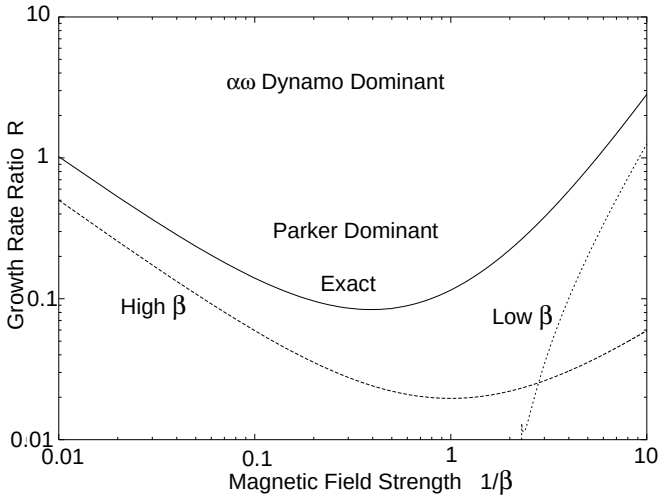

Figure 3.5: The growth rate ratio $\mathcal{R}_d$ on the disk surface $z = H$ as the function of the magnetic field strength $1/\beta$. The ratios with reduced formulas [Eqs. (3.20) and (3.21)] are also shown. In the early stage[$1/\beta < 1$, Eq. (3.20)], the Parker instability is dominant($\mathcal{R}_d < 1$). In the later stage[$1/\beta > 1$, Eq. (3.21)], the dynamo effect sets in by the central object activity($\mathcal{R}_d > 1$).

3.4 Radial Mass Spectrum of Accretion Disk

The radial mass spectrum of aggregated matter that may be organized as a result of nonlinear evolution of the MHD instabilities given in Sec. 3.3 for a protoplanetary accretion disk is now estimated from the characteristics of the magnetorotational and kinematic dynamo instabilities.

Two different types of density profiles are chosen and the mass spectra of these profiles are compared. First, it is assumed that the radial dependence of density $\rho(r, z)$ is parameterized by [80]

$$\rho = \rho_0(z) \left(\frac{r_0}{r} \right)^{\nu}. \tag{3.22}$$

The magnetic field strength $|\boldsymbol{B}|$ and pressure is assumed to be constant($T(r) = T_0(r/r_0)^{\nu}$) on the equatorial plane of the disk. The height of the disk H is redefined here for the global spectrum. The gravity in the z direction $g_z \simeq GMz/r^3$ is assumed, and the pressure equilibrium is solved in the z direction, which yields

$$H^2 = \frac{(1+\beta) r^3 C_s^2}{GM\beta} = H_0^2 \left(\frac{r}{r_0} \right)^{3+\nu} \tag{3.23}$$

and $\rho_0(z)/\rho_0(0) = P(z)/P(0) = B^2(z)/B_0^2 = \exp(-z^2/2H^2)$. Note that the Alfvén velocity $v_A = \sqrt{B^2/4\pi\rho}$ and the sound speed $C_s = C_{s0}(r/r_0)^{\nu/2}$ are constant in the z direction. Then, we integrate $\rho(r, z)$ in the z direction to estimate the average density $\bar{\rho}(r)$ at finite radius r,

$$\bar{\rho}(r) = \frac{1}{H} \int_{-\infty}^{\infty} \rho dz = \sqrt{\pi} \rho_0(0) \left(\frac{r_0}{r} \right)^{\nu}. \tag{3.24}$$

The total mass $M_s(r)$ between two Alfvén singular points in corotational coordinates, which is the typical scale length of the magnetorotational instability

in the radial direction, can be given by

$$M_s = 2\pi r\bar{\rho}H \times \frac{v_A}{A} = \frac{8\pi\sqrt{\pi}}{3}\frac{\rho_0 H_0 r_0 v_A}{A_0}\left(\frac{r}{r_0}\right)^{3-\nu/2}, \tag{3.25}$$

for pure azimuthal perturbation in a Keplerian disk. Typically it is considered $\nu = 2$ in an early stage of accretion disk evolution. In this case, the mass spectrum increases with r. This mass M_s is the maximum seed mass available from the MHD evolution between the two Alfvén layers separated by $\Delta r = v_A/A$.

Another, more specific, mass density model introduced by Okada et al. [22] assumes that magnetic field exists only in the azimuthal direction and that the density distribution with the azimuthal symmetry is obtained by integrating the equations of motion into the potential form,

$$\rho = \left(\frac{\max[\Phi_0 + 1/R - L^2/(2r^2), 0]}{K[\gamma/(\gamma-1)][1+\beta_0^{-1}r^{2(\gamma-1)}]}\right)^{1/(\gamma-1)}, \tag{3.26}$$

where

$$\Phi_0 = -\frac{1}{R} + \frac{L^2}{2r^2} + \frac{1}{\gamma-1}C_s^2 + \frac{\gamma}{2(\gamma-1)}v_A^2, \tag{3.27}$$

is the value of potential on the surface of the torus where the mass density $\rho = 0$, K is a dimensionless constant, $R = (r^2+z^2)^{1/2}$, L is the angular momentum, γ is the specific heat ratio, and $\beta_0 = 2K/F$ is the plasma β at $(r,z) = (r_0, 0)$, where F is a dimensionless constant. This potential density profile forms torus around the central object [22]. Since the Alfvén velocity is defined by $v_A^2 = F \times (\rho r^2)^{\gamma-1}$ and the sound speed $C_s^2 = K\gamma\rho^{\gamma-1}$ in this model, the mass spectrum of the maximum aggregated matter between the Alfvén resonance is given by

$$M_s = \frac{8\pi v_{A0}}{A_0}\left(\frac{r}{r_0}\right)^{2\gamma+1/2}\int_{z_-}^{z_+}\rho^\gamma dz, \tag{3.28}$$

where $z_{\pm} = \pm\sqrt{2r^2/(L^2 - 2r^2\Phi_0) - r^2}$. Thus, the radial dependence of M_s is determined by the factors Φ_0 and γ.

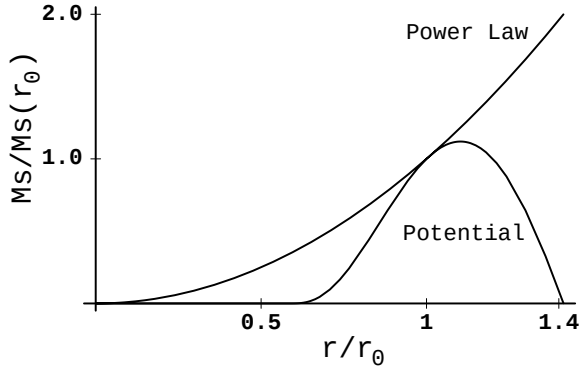

Figure 3.6: Mass spectrum of an accretion disk in the outer region($r > 1$AU). The horizontal axis indicates the radial distance from the rotating axis of the disk, in arbitrary unit. We plot the mass spectrum for two different density profiles, $\rho = \rho_0(r_0/r)^{\nu}$ and the profile given by equation (3.26).

The r dependence of those two mass spectra is shown in Fig. 3.6. For the power law model in Eq. (3.25), $\nu = 2$ and the other parameters are chosen to match the initial condition of the simulation done by Machida et al [15]. As described above, the mass spectrum increases with r if the density profile obeys a power law with $\nu < 6$. On the other hand, if the density profile is given by the potential density model in Eq.(3.26), there is a well defined maximum mess spectrum at some radius.

In the inner region($r < 1$ AU), the kinematic dynamo is predominant in determining the plasma turbulence. In this case, planetary formation is inhibited inside of the Roche limit $r_R = 2.456(\rho_{\odot}/\rho)^{1/3}R_{\odot}$, where $\rho_{\odot}$ and $R_{\odot}$ are the density and the radius of the central object, and ρ is the density of the accretion disk, respectively. For instance, if the density of the gas is $\rho = 10^{-10}$ g·cm^{-3} and central object has the solar density and radius($\rho_{\odot} = 1.41$ g·cm^{-3},

$R_\odot = 6.96 \times 10^5$ km), planetary formation is prohibited in the region $r_R \leq 1$ AU. If only the tidal force and self-gravitation are considered, the typical wavelength for exponential growth of density waves in the radial direction is

$$\lambda_c = \frac{2\pi^2 G\rho H}{\Omega^2}, \tag{3.29}$$

which yields the mass spectrum

$$M_s = 2\pi r\bar{\rho}H \times \lambda_c = \frac{4\pi^4 r_0^4 H_0^2 \rho_0^2}{M}\left(\frac{r}{r_0}\right)^{7-\nu}, \tag{3.30}$$

for the power law density model. For the potential density model in Eq. (3.26), the mass spectrum is

$$M_s = \frac{4\pi^3 G}{\Omega_0^2}\left(\frac{r}{r_0}\right)^3 \int_{z_-}^{z_+} \rho^2 dz \tag{3.31}$$

where the integral must be performed numerically to get the mass spectrum, $M_s(r)$.

Another characteristic wavelength is the width of dynamo eigenmodes. Stepinski et al. [19] showed the eigenmodes extend from the axis of the rotation to $r = 5 \sim 10H$. Since the height of the disk H is given by Eq. (3.23), the mass spectrum due to the dynamo effect for the power law model can be estimated in the form

$$M_s = 5 \times 2\pi r\bar{\rho}H = 10\pi\sqrt{\pi} r_0 r_0 H_0 \left(\frac{r}{r_0}\right)^{(5-\nu)/2}. \tag{3.32}$$

For the potential model, ρ is integrated over z to get the mass spectrum.

The mass spectra of those cases are shown in Fig. 3.7 with $\nu = 2$. In Fig. 3.7(a), the mass spectrum due to the the self-gravitation of gas is calculated. As Eq. (3.31) shows, the mass spectrum with power law density profile increases

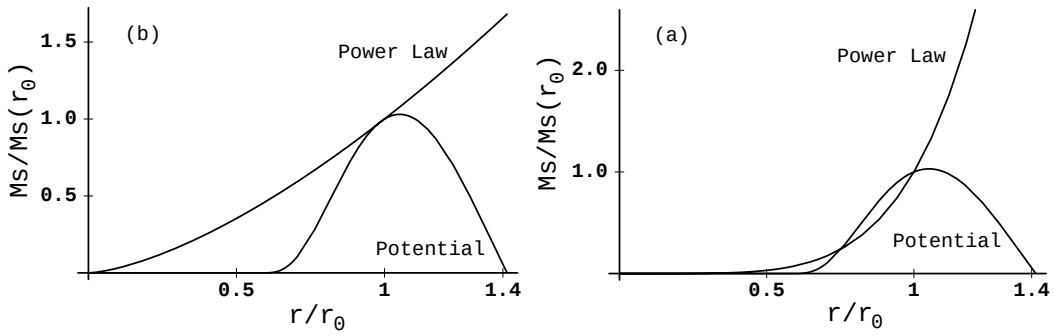

Figure 3.7: Mass spectrum of an accretion disk in the inner region($r < 1$AU). The horizontal axis indicates the radial distance from the rotating axis of the disk, in unit of r_0. Fig. 3.7a shows the spectrum due to the self-gravity of gas, and Fig. 3.7b shows the spectrum due to the magnetic dynamo. The spectra for two different density profiles are plotted, $\rho = \rho_0(r_0/r)^\nu$ and the density profile given by equation (3.26).

with r when $\nu \leq 7$. However, when the density profile is given by Eq. (3.26), the spectrum rises from $r \sim 0.65r_0$, has a peak at $r \simeq r_0$, and then decreases.

The mass spectra due to the magnetic dynamo are shown in Fig. 3.7(b). For the power law profile, the mass spectrum also increases with r when $\nu \leq 5$, and the potential model has a peak at $r \simeq 1.1r_0$. In both models, the mass accumulated by the magnetic dynamo effect is larger in inner region($r/r_0 < 1$) and the self-gravitation larger in outer region($r/r_0 > 1$). The self-gravitation effect may suppress further because of tidal force from fast sheared flow, and the magnetic dynamo play a important role for accumulation of the gas.

3.5 Numerical Simulation of Coupled Instabilities

The results of three-dimensional MHD simulations in a corotating reference frame is presented. The basic equation are ideal MHD equations in the rotating frame where the gas is stationary at $r = r_0$. In this frame $2\Omega(r_0)$ gives the

Coriolis acceleration. It is assumed that the curvature effect is negligible and the local cartesian coordinate system(x, y, z) is used. The code I use here is developed by Matsumoto [6](with the modifications noted below), which uses the modified Lax-Wendroff method [81]. This code is as same as that Chou used to show the Jeans-Parker instability [82].

A schematic of the simulation box is shown in Fig. 3.2. The bottom$(z = 0)$ and top$(z = H)$ of the box corresponds to the equatorial plane and surface of the disk, and uniform gravity is applied in the z direction. The initial shear flow is applied in the y direction, which corresponds to the flow in the azimuthal direction in the accretion disk case and magnetic field in the y direction supports fluid against the gravity. The periodic boundary in the x(radial) direction and a free boundary at $z = H$ are assumed. The boundary condition at $z = 0$ is antisymmetric for magnetic field, and symmetric for other field variables. The periodic boundary conditions in the y and z directions, and the shear boundary condition in the x direction are adopted [6, 45],

$$\begin{aligned} f(x, y, z, t) &= f(x + L_x, y - 2AL_x t, z, t) \\ v_y(x, y, z, t) &= v_y(x + L_x, y - 2AL_x t, z) + 2AL_x \end{aligned} \tag{3.33}$$

where L_x, L_y, L_z is the sizes of the simulation box in the x, y, z directions, respectively.

Simulation results are shown in Fig. 3.8 and Fig. 3.9, where plasma β is unity on the equatorial plane$(z = 0)$, and the adiabatic gas constant $\gamma = 1.05$ for nearly isothermal dynamics. Sinusoidal incompressible perturbation is the input, whose wavelength corresponds to $k_{mr} = v_A/A$ in x direction and $k_P(3.5)$ in y direction to the velocity field. The results of this local shearing

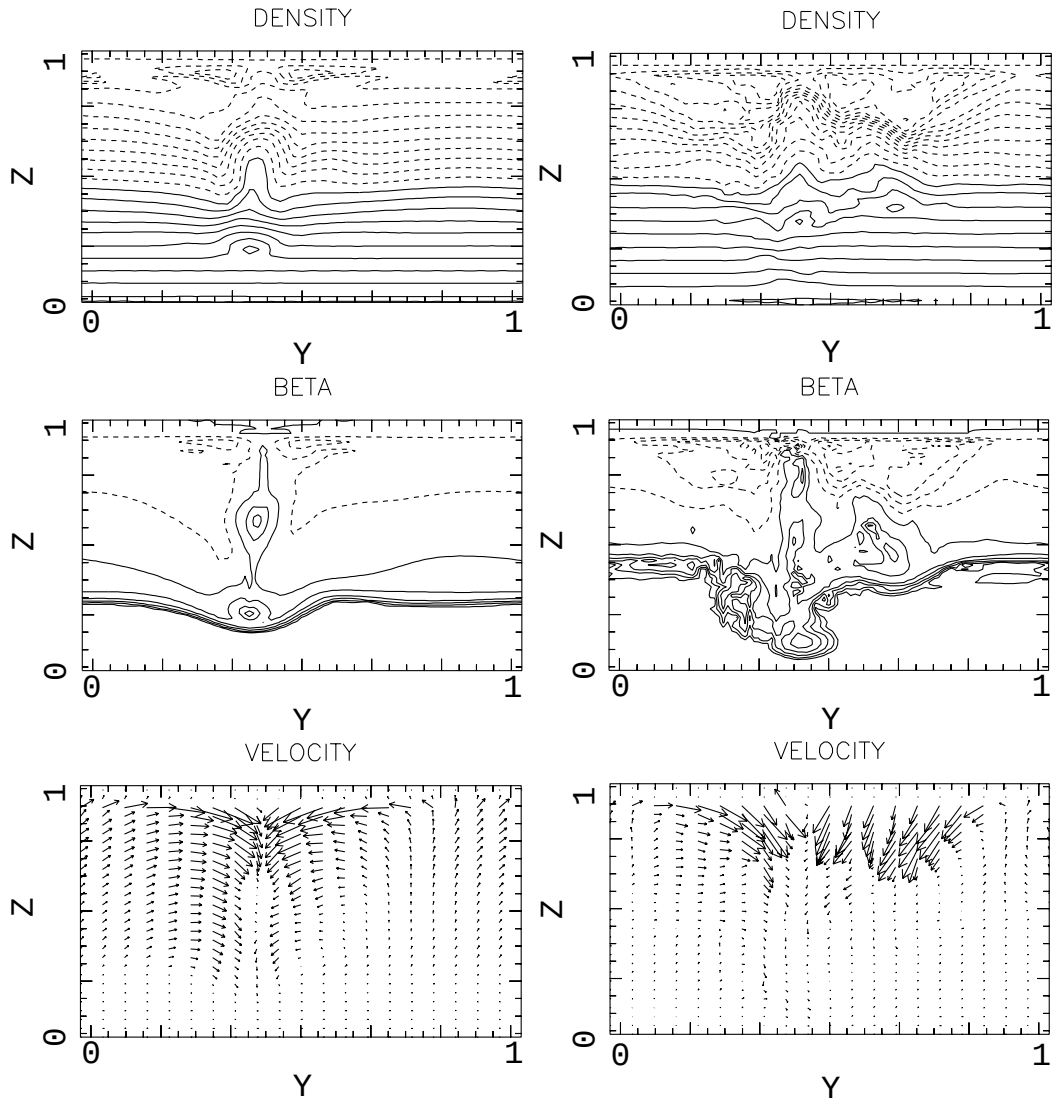

Figure 3.8: Contour plots of density ρ and plasma beta β, and velocity field projected to the plane $x = 0.625$ at $t = 2.05\Omega^{-1}$(left column) and $t = 2.93\Omega^{-1}$(right column). The contours of density are logarithmically spaced. The plots illustrate the evolution of magnetic loop and accretion of gas to the foot points of loops.

box simulation shows the same characteristics of the global simulations [15]. At $t = 2.05\Omega^{-1}$, the Parker instability creates magnetic loops in the azimuthal direction and plasma accretes to the foot points of loops. Plasma also accretes in

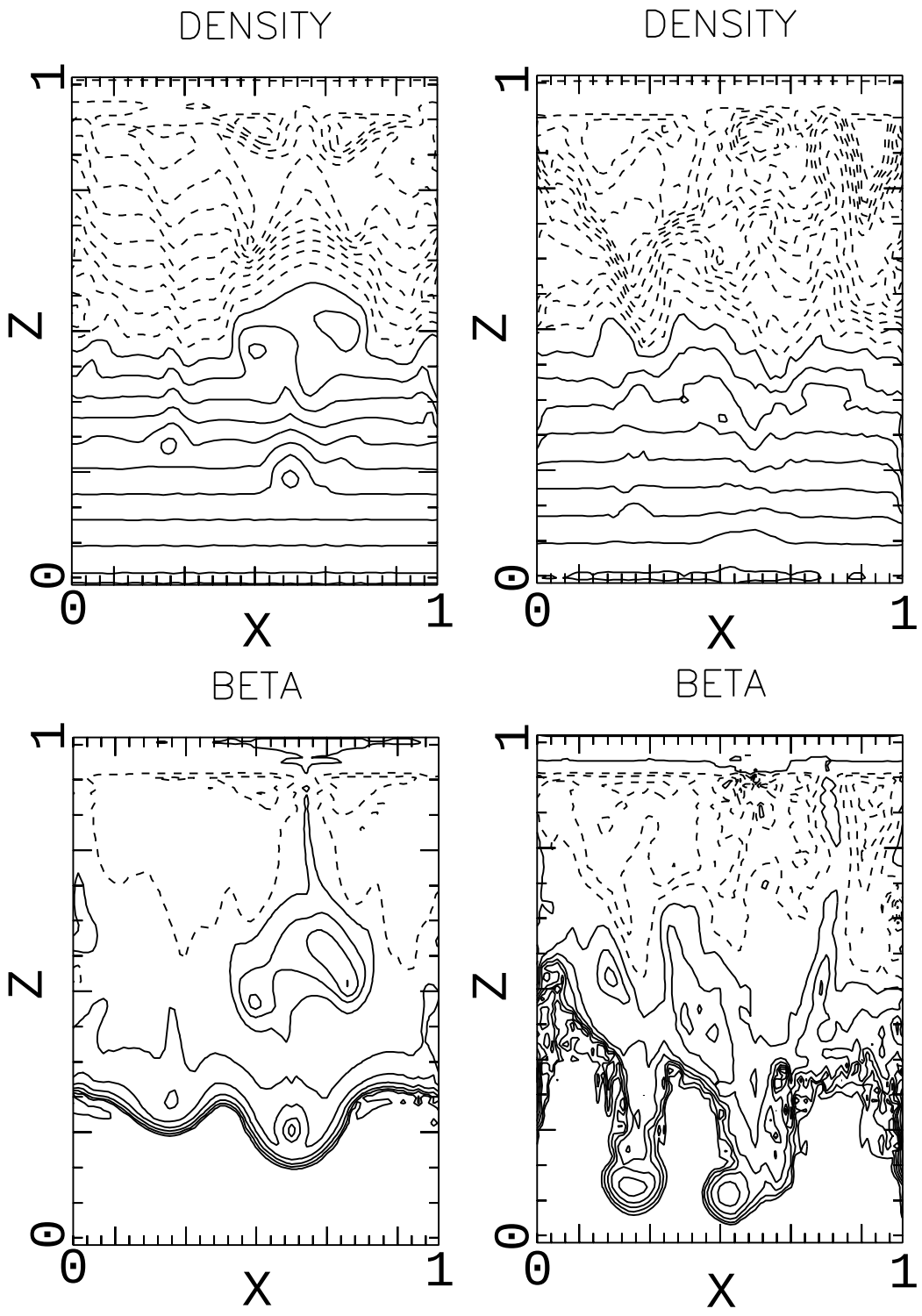
DENSITY
DENSITY
BETA
BETA
Z
X
0
1

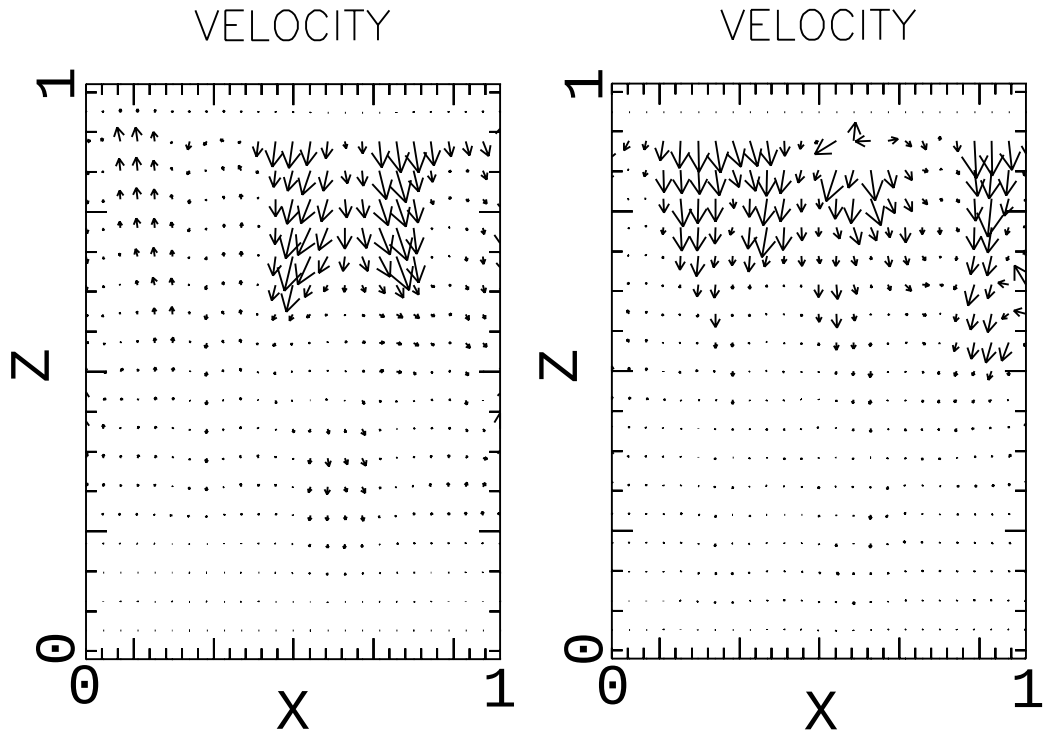

Figure 3.9: Contour plots of density ρ and plasma beta β, and velocity field projected to the plane $y = 0.5$ at $t = 2.05\Omega^{-1}$(left column) and $= 2.93\Omega^{-1}$(right column). The contours of density are logarithmically spaced. The plots illustrate the evolution of dense layer and blobs near the equatorial plane of accretion disk.

the radial direction due to the magnetorotational instability. The combination of these two instabilities makes high density stripe regions in the equatorial plane.

At later time($t = 2.93\Omega^{-1}$), the density at the bottom of the loops becomes larger and shows some dense blobs($\delta\rho/\rho \simeq 0.3$). Note that even though strong shear flows exist, blobs and spiral dense regions do not disappear due to phase mixing. Magnetic fields continuously escape through the top of the box because of the buoyancy of the flux tubes with higher values of the magnetic field, but the maximum strength of magnetic field increases because

magnetic field is continuously amplified by the magnetorotational instability.

Global simulations [15] showed that the competition between the magnetorotational and the Parker instability become quasi-periodic after some rotations. When the magnetic field becomes strong the dynamo process slows down and the Parker instability accelerates and vice-versa. In Fig (3.9), the simulation is terminated before it reaches the quasi-periodic state, but all the major features of the global simulation appear in the local simulation.

3.6 Laboratory Plasmas with Shear-flow Induced Structures

The "simulation" of the above processes of structure formation relevant to the planetary genesis in laboratory plasmas is considered. In tokamak plasmas, strong shear flows has been observed either due to the external drive(such as the neutral beam injection(NBI) [83,84]) or due to the spontaneous creation of flow drive mechanism [85,86]. In addition it appears possible to generate shear flows in laser irradiated targets [87].

For a plasma in tokamak, the gravitational force is replaced by the centrifugal force, which is created by the thermal velocity and/or flow in toroidal direction and is some substantial fraction ϵ of C_s,

$$g_z = \frac{(\epsilon C_s)^2}{R_t} \tag{3.34}$$

where R_t is the major radius of the torus. Then, the growth rate ratio $\mathcal{R}$ in Eq. (3.8) can be written in the form

$$\mathcal{R}_{toc} = \frac{2A\Omega R_t^2(1+\beta)^3(1-\sqrt{\beta})}{5\epsilon^4 C_s^2 \beta(2-3\sqrt{\beta})(5\beta/2-\sqrt{\beta}+1)}. \tag{3.35}$$

Since the toroidal flow velocity $v_\phi = \Omega R_t$ is equal to ϵC_s and $\beta \ll 1$, the tokamak $\mathcal{R}_{tok}$ can be reduced further to

$$\mathcal{R}_{tok} = \frac{A}{5\Omega}\frac{1}{\beta\epsilon^2}. \tag{3.36}$$

The value of β in a typical experiment is a few percent($\beta \sim 0.03$) in the core, and drops by factor of 10 to 20 near the wall. If the average value $\beta = 10^{-3} \sim 10^{-2}$ is assumed, and $\epsilon = 0.1$, $\mathcal{R}_{tok}$ becomes a function of the ratio A/Ω

$$\mathcal{R}_{tok} = \frac{A}{\Omega} \times 10^3 \sim 10^4. \tag{3.37}$$

The toroidal flow shear profile, and thus the flow shear parameter A, are known from the toroidal flow profile measured by the Doppler-shifts of co-rotating impurities. The hydrogenic working gas of the plasma rotates with the impurities due to the radiation, strong collision and friction between the two ion species. the details are in Zhu et al. [75]. The typical value of A is 100kHz. The toroidal rotation of the hydrogen plasma is driven by the neutral beam injection. In large tokamaks(JET, JT60U, DIIID), the toroidal velocity reaches $200 \sim 300$km/s, which yields $\Omega \sim 100$kHz. The Alfvén frequency is comparable since $k_\| \sim (1/q)R \sim 10^{-3}\text{cm}^{-1}$ and $v_A = \sqrt{B_p^2 + B_T^2}/\sqrt{4\pi\rho} \sim B_T/\sqrt{4\pi\rho} \sim 3 \times 10^8$cm/s. For a review of the toroidal Alfvén eigenmode(TAE) and continuum, see [52, 88–91]. The estimated value of $\mathcal{R}_{tok}$ is about $10^3 \sim 10^4$ for the transport barrier region. However, large values of $\mathcal{R}_{tok}$ does not mean plasma is turbulent, but means that the Parker instability grows slowly because of the strong magnetic field[see Eq. (3.4)]. The details of the turbulent transport from both rotating shear, magnetic shear and the thermal gradient are complex in tokamaks. Shear flow can be either stabilizes or destabilizes depending on the details [92]. Other electrostatic shear flow driven instabilities are possible [93].

Another problem is to maximize the growth rate of the magnetorotational instability by equalizing the Alfvén frequency ω_A to the rotating speed Ω. For tokamak devices, poloidal magnetic field is ~ 0.1T and density n is $5\times 10^{13}\mathrm{cm}^{-3}$, which yields the effective Alfvén velocity of the order of 10^2km/s. Thus, the typical length of the magnetorotational instability in the poloidal direction [6],

$$\lambda_{mr} = \frac{v_{Ap}}{A} \simeq \frac{R_t}{\epsilon\sqrt{\beta}} \ll R_t, \tag{3.38}$$

is the order of 10^4cm, where $v_{Ap} = B_p/\sqrt{4\pi\rho}$ is the Alfvén velocity due to the poloidal magnetic field. The typical wavelength of the Parker instability in the toroidal direction is

$$\lambda_P = 2\pi/k_P = \frac{4\pi(1+\beta)}{\beta^{3/4}(2-3\sqrt{\beta})^{1/2}}\frac{R_t}{\epsilon^2}, \tag{3.39}$$

whose value is 10^5cm.

Dimensionless measure of the magnetic(Maxwell stress) viscosity coefficient μ_B caused by the magnetorotational instability is given by [6],

$$\mu_B = -\frac{\langle \delta B_x \delta B_y \rangle}{4\pi\rho C_s^2} < \frac{\langle \delta B^2 \rangle}{4\pi\rho C_s^2}. \tag{3.40}$$

Substituting all the variables in eq. (3.40), the magnetic viscosity in tokamak device is estimated to be $\mu_B \ll 0.01$ due to the low level of $\langle \delta B^2 \rangle$ in the system [94].

Next, the possibility of laser simulation plasma experiments is considered. A schematic view of a simulation experiment is shown in Fig. 3.10 [87]. Though it may not be easy to apply magnetic fields to the target, strong fields may be generated by applying electric current to a target perpendicular to the direction of laser injections to create magnetic field in the azimuthal direction.

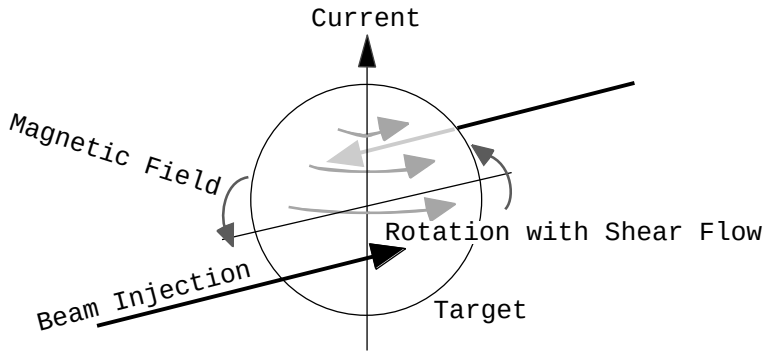

Figure 3.10: A schematic view of a laser experiment. Electric current is apply parallel to the rotation axis to create magnetic field in the azimuthal direction. The directions of laser injection are slightly out of axis to create shear flow in the azimuthal direction. The injected laser compresses the target radially to make target Parker unstable.

The injection directions of lasers are offset from the symmetry axis, so that the target obtains angular momentum from the laser beams. The target is nonuniform to create a sheared rotation in the equatorial plane. Since the target is Rayleigh-Taylor unstable due to the imploding pressure of the laser and magnetorotational unstable due to the sheared rotation and magnetic field, one should be able to observe how global structure grows experimentally if variables are properly chosen.

A critical condition for laser-space plasma experiments is to make the equations of motion invariant under the scale transformation [77]:

$$\begin{aligned} \rho_d &= a_1 \rho_e, \\ p_d &= a_2 p_e, \\ h_d &= a_3 h_e, \\ \tau_d &= a_4 \tau_e, \end{aligned} \tag{3.41}$$

where ρ, p h and τ are characteristic values of density, pressure, spatial scale

and time, respectively, and subscripts d and e indicate those values are for the accretion disk(d) or the experiment(e). The ratios a_1, a_2, a_3 are determined from those parameters. Under the transformation, the characteristic values of time scale τ, magnetic field B, and angular frequency Ω are transformed as

$$\begin{aligned} \tau_d &= \sqrt{\frac{a_1}{a_2}} a_3 \tau_e \equiv a_4 \tau_e, \\ B_d &= a_2^{1/2} B_e, \\ \Omega_d &= \sqrt{\frac{a_2}{a_1}} \frac{1}{a_3} \Omega_e = \frac{1}{a_4} \Omega_e. \end{aligned} \tag{3.42}$$

First, the ranges of a_1 and a_2 are determined from the relative density and magnetic field strengths. The typical strengths of magnetic field are $B_d = 10^{-3}\text{G} \sim 1\text{G}$ and $B_e = 1\text{G} \sim 1\text{T}$, which yields $a_2 = 10^{-14} \sim 10^0$. Since the typical number density of a protoplanetary accretion disk is $n = 10^4 \sim 10^6 \text{cm}^{-3}$ whose content is mostly hydrogen($\rho_d = 10^{-20} \sim 10^{-18} \text{g/cm}^3$) and that of target is $\rho_e = 1 \sim 10 \text{g/cm}^3$, the ratio a_1 is the order of $10^{-21} \sim 10^{-18}$. The pressure of the disk is estimated by assuming its temperature $T \sim 100\text{K}$, which yields $p_d = C_s^2 \rho / \gamma = 10^{-11} \sim 10^{-8}$ Pa and an experiment $p_e = p_d / a_2 = 10^{-11} \sim 10^6$ Pa.

Next, the range of a_2 is determined again, from an analysis of the typical scale length and time scale rather than the magnetic field. The typical scale length of an protoplanetary disk can be determined by the distance between the Alfvén singularities in corotational frame [63],

$$h_d \sim \frac{v_A}{A} = \frac{B}{\sqrt{4\pi\rho} A} = 10^{16} \sim 10^{21} \text{cm}, \tag{3.43}$$

where $A = 3\Omega/4$ and $\Omega = 10^{-9} \sim 10^{-7}$ s^{-1} are used, whose period is $10 \sim 10^3$ yr. For laser experiments, $h_e = 10^{-4} \sim 10^{-2}$cm, which yields $a_3 = 10^{18} \sim 10^{25}$.

The typical time scale of accretion disk evolution is estimated by the growth rate of the magnetorotational instability,

$$\tau_d = \frac{1}{\omega_A} \sim \frac{1}{\Omega} = 10^7 \sim 10^9 \text{s}. \tag{3.44}$$

The typical time scale of experiments is $\tau_e = 10^{-8} \sim 10^{-2}$ s, which makes the time scaling factor $a_4 \sim 10^{11} \sim 10^{17}$. Since the pressure is $\propto \rho(T/m) \sim a_1(a_3/a_4)^2 \sim a_2$ so that from the square-time scaling one finds

$$a_2 = a_1 \left(\frac{a_3}{a_4}\right)^2, \tag{3.45}$$

to make the equation of motion invariant under the scaling transformation, the range of a_2 is $10^{-19} \sim 10^0$(this large range is due to the square in Eq.[3.45]), which overlaps with the range of a_2 calculated from magnetic field strength. Thus, it is found that a laser experiment for an accretion disk may be achieved in the range $10^{-14} < a_2 < 10^0$.

The rotation frequency for experiments Ω_e is given by

$$\Omega_e = a_3\sqrt{\frac{a_1}{a_2}}\Omega_d = 10^2 \sim 10^{10}\Omega_d. \tag{3.46}$$

A simulation regime would be $\Omega_e \sim 10^2 \text{s}^{-1}$, which correspond to $B_e \sim 100$G, $P_e \sim 10^{-6}$Pa, $h_e \sim 10^{-4}$cm, $\tau_e \sim 10^{-6}$s.

This scale transformation are also applied to active galactic nuclei(AGNs). Typical ranges of variables for AGNs are $B_{AG} = 10^{-3}\text{G} \sim 10^{-1}$G, $\rho_{AG} = 10^5 \sim 10^6 \text{g/cm}^3$, $T_{AG} = 10^3 \sim 10^4$K, $M_{AG} = M_\odot \times 10^8$, $r_{AG} = 10 \sim 100$AU. Substituting all the variables to eqs.(3.41) and (3.42), we can estimate realistic experimental values as $B_e = 10^{-1}$G, $\rho_e = 10\text{g/cm}^3$, $P_e = 10^9 \sim 10^{11}$Pa, $h_e \sim 10^{-2}$cm, $\tau_e \sim 10^{-2}$s, and $\Omega_e = 10\text{s}^{-1}$. The comparison of the estimated values are shown in Table 3.6.

	Planetary	AGN	Tokamak	Laser	
				Planetary	AGN
L(cm)	$10^{10} \sim 10^{11}$	$10^{13} \sim 10^{15}$	$10^{3} \sim 10^{4}$	$10^{-4} \sim 10^{-2}$	
t(s)	$10^{7} \sim 10^{9}$	$10^{6} \sim 10^{12}$	$10^{-5} \sim 10^{-4}$	$10^{-8} \sim 10^{-2}$	
P(Pa)	$10^{-6} \sim 10^{-3}$	$10^{9} \sim 10^{11}$	$10^{3} \sim 10^{4}$	$10^{-9} \sim 10^{-6}$	$10^{9} \sim 10^{11}$
ρ(g/cm^3)	$10^{-18} \sim 10^{-20}$	$10^{5} \sim 10^{6}$	$10^{-11} \sim 10^{-10}$	$1 \sim 10$	
B(G)	$10^{-3} \sim 1$	$10^{-3} \sim 10^{-1}$	10^{3}	10^{2}	10^{-1}
T(eV)	10^{-2}	$10^{-1} \sim 1$	10^{4}	$10^{-2} \sim 10^{-1}$	1
a(cm/s^2)	$10^{-4} \sim 10^{2}$	$10^{-11} \sim 10^{-6}$	$10^{10} \sim 10^{13}$	$10^{-8} \sim 10^{-2}$	$10^{11} \sim 10^{16}$
$\mathcal{R}^{1/2}$	$1 \sim 10$	$10^{6} \sim 10^{9}$	$10^{1} \sim 10^{2}$	$\ll 1$	

Table 3.1: Typical quantities of accretion disks and experimental plasmas. L: scale length, t: typical time scale, P: typical pressure, ρ: density, B: magnetic field strength, T: typical temperature, a: acceleration, $\mathcal{R}$: growth rate ratio.

In both cases, the ratios $\mathcal{R}$ and $\mathcal{R}_d$ may be small. It is not easy to adjust the rotation frequency and the shear rate of the target to the ideal values. The Parker instability is relatively easy to control, since the pressure of the laser directly makes the target Parker-unstable. The resulting gas buoyancy may be too strong to couple either the magnetorotational instability or kinematic dynamo. Thus, the tokamak simulation would appear more straightforward to create for the accretion disk.

3.7 Discussion

The combined effects of the magnetorotational, kinematic dynamo, and Parker instabilities gives rise to density blobs in an accretion disk, which may contribute to the structure formation in accretion disks prior to the self-gravitational instability. The mass spectrum of such aggregations has been calculated from the typical wavelength of the magnetorotational instability, self gravitation, and magnetic dynamo, indicating the accumulation of the density in the radial direction. The similarity of mass spectra by the magnetorotational instability

and Jeans(self-gravitational) instability indicates that the magnetorotational instability can create similar mass spectra predicted from the conventional theory in shorter time scale, which may solve three observational questions addressed in §3.1.

By the scale transformations of the equation of motion, it is found that this coupling instability regime may be observable experimentally in laboratory plasmas to simulate the structure formation process in protoplanetary disks. The azimuthal dependence of the coupled instability in the nonlinear phase remains to be an issue of investigation.

To show how the theoretical estimation match with observations, I choose the dust ring around ϵ edriani [95] as an example. As showed in Chapter 2, the wave number directional dependence of the magnetorotational instability arises only from the ratio $q = k_\theta^2/k_z^2$, where k_θ is the wave number in the azimuthal direction($k_\theta = k_y$), and k_z is in the direction of the rotation axis [63]. By using the radius of the disk r and azimuthal mode number m, k_θ is estimated as $k_\theta = m/r$. For thick disk, k_z can be estimated by π divided by a half height of the disk H and a vertical mode number n as $k_z = n\pi/H$. The ratio q is then given by

$$q = \left(\frac{mH}{\pi n r}\right)^2 . \tag{3.47}$$

The dust ring around ϵ edriani [95] is observed to have an azimuthal structure with mode number $m = 5 \sim 6$. The ratio between the height to the radius of the disk is assumed as $H/r \sim 1/3$, and estimate $q = 4/9$ for $n = 1$, which agrees with the analytical value of q with maximum growth rate(see Fig./ 2.5). Thus, it is plausible that gas in the disk is accumulated to a ring with radius $r \sim 60$ AU by the magnetorotational instability and that the Parker

instability couples to the magnetorotational instability to explain the creation of an azimuthal structure in ϵ edriani.

After blobs are created in a accretion disk, only stable ones remain to be the seeds of planets. With respect to the nonlinear evolution of the seeding process, a work by Horton & Smith [76] may be instructive to the present problem. They showed that the coupling of radial plasma gradient to the centrifugal and Coriolis forces gives rise to solitary monopole and dipole vortices in the sheared rotation of the Io plasma torus around Jupiter. The dynamics is through the drift wave-Rossby wave process [96]. The maximum vortex radius R_v is given approximately by velocity shear length $R_v \simeq -(d \ln \Omega/dr)^{-1} = -r\Omega/2A$, which may be greater or smaller than the blob size created by the coupling of the magnetorotational and Parker instabilities, depending on how strong the magnetic field is. Since the typical wavelength of the magnetorotational instability is $\lambda_{mr} = \omega_A/(Ak_y) \sim 1/k_P$ and the Parker instability $\lambda_P = 8\pi H/\sqrt{3} \sim H$, the typical size of the blob is the height of the disk in both the radial and azimuthal directions, which is of the order of 1 AU. If the blob size is smaller than R_v, the blobs are stable and grow by interacting with each other to give rise to planetesimals. Once stable blobs are created in the disk, they would be subject to the Jeans and Jeans-Parker instabilities [82]. If the blob size is larger than the Jeans and Jeans-Parker instabilities, these instabilities may start immediately from the blob formation. These further facilitate the structure formation. In this second stage, the differential rotation may be slower than that in a Keplerian disk so that the Jeans instability can create a larger structure against phase mixing in the shear flow. When the typical length of the blobs exceeds

the Jeans wavelength λ_J,

$$\lambda > \lambda_J = \frac{2\pi C_s}{\sqrt{4\pi G\rho}}, \tag{3.48}$$

the Jeans instability sets in. However, λ_J is $10^3 \sim 10^4$ AU with $T = 100$K and $n = 10^4/\text{cm}^3$, indicating that density should be higher at least in dense regions for the Jeans instability.

Difficulty of huge planetary formation like the Jupiter and the comparable ages of the Earth and Sun(see §3.1) can solve if the structure formation can be accelerated by any mechanism other than the Jeans instability. As I showed in §3.2, magnetorotational instability can accelerate the structure formation in the radial direction, whereas the Parker instability create a structure in the azimuthal direction. Furthermore, the magnetorotational instability accelerates the accretion of a disk by transferring the angular momentum outward(see Chapter 2). Thus the total effect of these MHD instabilities can accelerate the protoplanetary formation, which may solve these two questions.

As I showed in §3.3, the structure formation via MHD instabilities depend on the existence of magnetic field, and the distribution of magnetic field in a protoplanetary disk affects the resulted mass spectra. The potential density distribution (3.26) only assumes the azimuthal symmetry, and two parameters Φ_0 and γ can be chosen arbitrarily, which means that the mass spectra may have maximum at any radius [22]. Even though steady state solution may not be realistic, the calculated mass spectra may explain the existence of huge exosolarplanets.

Gas particles(grains) in a accretion disk are formed with a distribution over radius a with density $n_d(a) \sim 1/a^7$ [97]. They are mostly charged [98,99].

Charged dust particles with large mass may give rise to the strong Hall electric field, which breaks the "frozen-in" law of the magnetic field and separates dusty plasma from electron-ion plasma [100], whereas smaller grains are more tightly frozen to the field [101]. Thus, after planetesimals are created, the effect of dusty plasma becomes important.

In Sec. 3.6, the possibility of experiments of analogous phenomena in laboratory plasmas has been discussed. Though this is an excellent case for the creation of a database for planetary formation, there remain several problems in achieving scaling. First, radiation pressure may be stronger in laser plasmas than in protoplanetary accretion disks(perhaps appropriate to the radiation pressure in disks with AGNs). Since the temperature of the protoplanetary accretion disk gas is typically low($T \sim 10^2$K), the radiation pressure is neglected in the calculation and simulation. However, the temperature in the analog laser experiments is typically high($10 \sim 100$eV) so that the radiation pressure is not negligible. Second, the control of shear flows is challenging in laboratory plasmas for its role in the transport of angular momentum although recent progress with RF heated plasma has been made [102–104]. In tokamak devices, shear flows are created by unbalanced natural atomic beam injection(NBI) and by radio frequency(RF), and maintained by plasma itself in ohmic heating. To create near Keplerian shear flows in the device, the injection angle of NBI, external magnetic field, and plasma density should be carefully chosen. In laser plasmas, shear flows may be created by injected laser from opposite direction, producing a torque on the target pellet. Uniform sheared flow is difficult to create because of the inhomogeneity of laser irradiation to a target. Despite these difficulties, analog experiments are important provide database for non-

linear evolution of accretion disks with large density and magnetic field ranges. Laboratory analog simulation always include more space-time scales and physical effects than possible with digital computer simulations. Our theoretical estimations can be applied to not only in protoplanetary disks and AGNs, but also any accretion disks such as accretion disks around dwarf novae and black holes. Analog experiments of those disks are also possible. Although these analog simulation experiments I suggested in this chapter is purely theoretical, simulation experiments may show more solid answers to the questions addressed in §3.1. If the technical difficulties can be solved, we can simulate more realistic accretion disks by experiments than three-dimensional computer simulations.

Chapter 4

The Coupling of the Magnetorotational and Parker Instabilities

4.1 Introduction

As stated in §3.3, the coupling of the magnetorotational and Parker instabilities play a important role in the structure formation in protoplanetary disks. Magnetic field in a disk is enhanced by the magnetorotational instability [3, 4], and the magnetic field energy is extracted by the Parker instability [16, 17]. However, even when magnetic field initially has only an azimuthal component, it will expanded due to sheared flow and magnetic buoyancy, which eventually creates complex structure and makes the disk turbulent. Three dimensional simulations [15, 45] showed complex structures are created in accretion disks. Non-eigenmode analysis [24] and coherent-wave solution analysis [23] do not fully resolve the coupling of the magnetorotational and Parker instabilities.

In §3.3, the growth rate ratio is estimated solely by non-coupled effects of the magnetorotational and the Parker instability. More accurate criteria for the structure formation can be given only by analyzing the coupling of these two instabilities. In this chapter, the linear analysis of the coupled magnetorotational-Parker instability is performed in the co-rotating frame with uniform gravity, which is provided by a central object. If the vertical gravity

is zero, the wave equation is proven to be the same as Eq. 2.6 in §2.2.

4.2 Wave Equation for the Coupling Instability

The basic ideal MHD equations in the co-rotating frame with angular velocity $\boldsymbol{\Omega}$ and uniform gravity $\boldsymbol{g}$ are

$$\begin{aligned} \frac{\partial \rho}{\partial t} + \nabla \cdot (\rho \boldsymbol{V}) &= 0, & (4.1) \\ \frac{\partial \rho \boldsymbol{V}}{\partial t} + \nabla \cdot (\rho \boldsymbol{V}\boldsymbol{V}) &= -\nabla P + \frac{(\nabla \times \boldsymbol{B}) \times \boldsymbol{B}}{4\pi} \\ &- \rho \boldsymbol{g} + 2\rho \boldsymbol{V} \times \boldsymbol{\Omega} + \rho(\boldsymbol{\Omega} \times \boldsymbol{r}) \times \boldsymbol{\Omega}, & (4.2) \\ \frac{\partial \boldsymbol{B}}{\partial t} &= \nabla \times (\boldsymbol{V} \times \boldsymbol{B}), & (4.3) \end{aligned}$$

where $\boldsymbol{g}$ has not only the radial component but also the axial component g_z in this chapter. Incompressibility is assumed again,

$$\nabla \cdot \boldsymbol{v} = 0, \tag{4.4}$$

which prohibits compressible grow of the Parker instability. However, in the linear stage, the Parker instability can grow in an incompressible fluid by exchanging heavier element with lighter element of fluid, and only this type of the Parker instability is considered here. The local cartesian coordinates (x, y, z) is adopted again, with flow shear $v_{y0} = -2Ax$ and the angular velocity in the z direction, $\boldsymbol{\Omega} = \Omega \hat{z}$. The fluid is assumed to be bounded below by a fixed boundary $z = 0$, which corresponds to the equatorial plane of the disk.

An isothermal hydrostatic equilibrium is adopted, which requires the z-dependence in the unperturbed density ρ_0 and the magnetic field in y direction B_{y0} and z direction B_{z0} as:

$$\rho_0 = \rho_0 \exp\left(-\frac{z}{H}\right), \tag{4.5}$$

$$B_{y0} = B_0 \exp\left(-\frac{z}{2H}\right), \tag{4.6}$$

$$B_{z0} = 0, \tag{4.7}$$

in order to satisfy the equation of motion (4.2) in z direction

$$\frac{d}{dz}\left(P + \frac{B_0^2}{8\pi}\right) + \rho g_z = 0, \tag{4.8}$$

and $\nabla \cdot \boldsymbol{B} = 0$. Here, $P(z) = P_0 \exp(-z/H)$ is the pressure, and H is the height of the disk, which is given by

$$H = \frac{C_s^2}{\gamma g_z}\left(1 + \frac{1}{\beta}\right), \tag{4.9}$$

where the sound speed

$$C_s^2 = \frac{\gamma P}{\rho_0}, \tag{4.10}$$

and the plasma beta

$$\beta = \frac{8\pi P}{B_0^2}, \tag{4.11}$$

are constant. The strength of uniform gravity in the z direction g_z is then determined by Eq. (4.9). In the unperturbed state, other components of the velocity and magnetic field are assumed as $v_{x0} = v_{z0} = B_{x0} = 0$.

The first order equations are then given by

$$\frac{d\rho}{dt} + (\boldsymbol{v} \cdot \nabla)\rho_0 = 0, \tag{4.12}$$

$$\rho_0 \frac{d\boldsymbol{v}}{dt} + \rho_0(\boldsymbol{v} \cdot \nabla)\boldsymbol{v}_0 - \rho_0(\boldsymbol{v} \times \boldsymbol{\Omega}) = -\nabla(p + \frac{\boldsymbol{B} \cdot \boldsymbol{b}}{4\pi}) + \frac{(\boldsymbol{B}_0 \cdot \nabla)\boldsymbol{b}}{4\pi} + \frac{(\boldsymbol{b} \cdot \nabla)\boldsymbol{B}_0}{4\pi} - \rho \boldsymbol{g}, \tag{4.13}$$

$$\frac{d\boldsymbol{b}}{dt} = (\boldsymbol{B}_0 \cdot \nabla)\boldsymbol{v} + (\boldsymbol{b} \cdot \nabla)\boldsymbol{v}_0 - (\boldsymbol{v} \cdot \nabla)\boldsymbol{B}_0. \tag{4.14}$$

Then consider solutions of the form [17]

$$v_i = C_s V_i(x, \omega) \exp\left(\mathrm{i}k_y y + \mathrm{i}k_z z + sz/2H\right),$$

$$b_i = B_0 B_i(x, \omega) \exp\left(\mathrm{i}k_y y + \mathrm{i}k_z z + (s-1)z/2H\right). \tag{4.15}$$

where the parameter s is to be chosen later to satisfy the fixed boundary condition at $z = 0$. The Laplace transform (2.5) is employed for time dependence of the perturbations.

It is convenient to introduce dimensionless parameters here. Since the frequency is always Doppler-shifted because of the sheared flow, the normalized Doppler-shifted frequency is given by $\Omega_D(x) = H\omega_D/C_s$, where $\omega_D = \omega + 2Ak_yx$. Other parameters can be also normalized in a similar fashion,

$$K_i = k_iH, \tag{4.16}$$

$$\Omega_n = \frac{\Omega H}{C_s}, \tag{4.17}$$

$$A_n = \frac{AH}{C_s}, \tag{4.18}$$

$$\Omega_A^2 = \frac{2K_y^2}{\beta\gamma}, \tag{4.19}$$

which represent the normalized wave number, angular frequency, the Oort's constant, and the Alfvén frequency, respectively. Then the homogeneous parts of the induction equations are

$$-\mathrm{i}\Omega_D B_x = \mathrm{i}K_yV_x, \tag{4.20}$$

$$-\mathrm{i}\Omega_D B_y = \mathrm{i}K_yV_y - 2A_nB_x + \frac{1}{2}V_z, \tag{4.21}$$

$$-\mathrm{i}\Omega_D B_z = \mathrm{i}K_yV_z. \tag{4.22}$$

Eliminating B_i from the equations of motion leads to the simple matrix form

$$\nabla\left(P + \frac{\boldsymbol{B}\cdot\boldsymbol{b}}{4\pi}\right) = \begin{pmatrix} \alpha(x) & \beta(x) & 0 \\ \gamma(x) & \alpha(x) & 0 \\ 0 & 0 & \eta(x) \end{pmatrix} \begin{pmatrix} V_x \\ V_y \\ V_z \end{pmatrix} \times \exp\left(\mathrm{i}\omega t + \mathrm{i}k_y y + \mathrm{i}k_z z + (s-2)z/2H\right), \tag{4.23}$$

where

$$\begin{aligned}
\alpha &= \mathrm{i}\Omega_D + \frac{\Omega_A^2}{\mathrm{i}\Omega_D}, \\
\beta &= 2\Omega_n, \\
\gamma &= -2(\Omega_n - A_n) - \frac{2A_n\Omega_A^2}{\Omega_D^2}, \\
\eta &= \mathrm{i}\Omega_D + \frac{\Omega_A^2 - 1}{\mathrm{i}\Omega_D}.
\end{aligned} \tag{4.24}$$

Since the subsonic fluid motion is incompressible, taking the rotation of the equations of motion for eliminating pressure term is acceptable. By taking the rotation of (4.23) for eliminating the pressure term, and substituting velocity to the equation of continuity

$$V_x' + \mathrm{i}K_y V_y + (\mathrm{i}K_z + s/2)V_z = 0, \tag{4.25}$$

yields the wave equation

$$\begin{aligned}
V_x'' + \left[-\frac{\mathrm{i}K_y\beta}{\alpha} + \frac{\gamma(K_y^2\eta + K_{zm}^2\alpha)}{\mathrm{i}K_y\alpha\eta} + \frac{\alpha'}{\alpha} + \log\left(\frac{\mathrm{i}K_y\eta}{K_y^2\eta + K_{zm}^2\alpha}\right)' - \frac{\alpha K_{zm}^2}{\mathrm{i}K_y\eta} \right] V_x' \\
+ \left[-\frac{K_y^2\eta + K_{zm}^2\alpha}{\eta} + \frac{\beta\gamma K_{zm}^2}{\alpha\eta} + \frac{\gamma'(K_y^2\eta + K_{zm}^2\alpha)}{\mathrm{i}K_y\alpha\eta} - \frac{\alpha' K_{zm}^2\gamma}{\mathrm{i}K_y\eta\alpha} \right. \\
\left. - \frac{\gamma K_{zm}^2}{\mathrm{i}K_y\eta}\log\left(\frac{\mathrm{i}K_y\eta}{K_y^2\eta + K_{zm}^2\alpha}\right)' - \left(\frac{\gamma K_{zm}^2}{\mathrm{i}K_y\eta}\right)' \right] V_x = 0,
\end{aligned} \tag{4.26}$$

where $V_i' = (\partial V_i/\partial x)/H$, and K_{zm} is a modified wavenumber in the z direction, given by $-K_{zm}^2 = (\mathrm{i}K_z + s/2)(\mathrm{i}K_z + (s-2)/2)$. In order to satisfy the boundary conditions on the equatorial plane, we must take $s = 1$ and $K_{zm}^2 = K_z^2 + 1/4$.

Preliminary results are obtained from examining the wave equation (4.26). If $g = 0$, $\alpha = \eta$ and $K_{zm}^2 = K_z^2$. Then the differential equation is reduced to the pure magnetorotational case,

$$V_x'' + \frac{\alpha' - \mathrm{i}K_y(\beta + \gamma)}{\alpha} V_x' + \left(-K^2 - \frac{\mathrm{i}K_y\gamma'}{\alpha} + \frac{K_z^2\beta\gamma}{\alpha^2} \right) V_x = 0, \tag{4.27}$$

where $K^2 = K_y^2 + K_z^2$, which is identical to Eq. (2.6).

The another limit can be examined if the background flow does not have shear, i.e. $A = 0$. In this case, all the x-differential terms in the coefficients of the wave equation (4.26) and the Doppler-shift effect vanish, $\Omega_D = \Omega$. Thus Fourier transform can be employed in the x direction by introducing $K_x = k_x H$, and Eq. (4.26) is reduced to the Parker dispersion relation with uniform flow,

$$-K_x^2 + \left[\frac{K_y\beta}{\alpha} + \frac{\gamma(K_y^2\eta + K_{zm}^2\alpha)}{K_y\alpha\eta} - \frac{\alpha K_{zm}^2}{K_y\eta}\right]K_x - \frac{K_y^2\eta + K_{zm}^2\alpha}{\eta} + \frac{\beta\gamma K_{zm}^2}{\alpha\eta} = 0. \tag{4.28}$$

The resonances occur at the Alfvén frequency and the the Brunt-Väisälä frequency in the atmospheric science [26],

$$\Omega^2 = \Omega_A^2, \quad \Omega^2 = \Omega_A^2 - 1, \tag{4.29}$$

which can be reduced further by taking $\boldsymbol{B} = 0$, which indicates one root is always unstable to convection because of the unstable stratification of the incompressible fluid. Note that the background flow does not affect the stabilization.

Singularities of Eq. (4.26) indicate where the resonance occurs. There are six singular points of Eq. (4.26) in total,

$$\Omega_D^2 = \Omega_A^2, \quad \Omega_D^2 = \Omega_A^2 - 1, \quad \Omega_D^2 = \frac{K_y^2 + K^2\Omega_A^2}{K^2}, \tag{4.30}$$

which can be rewritten as

$$\omega_D^2 = \omega_A^2, \quad \omega_D^2 = \omega_A^2 - \omega_g^2, \quad \omega_D^2\frac{k_y^2\omega_g^2 + k^2\omega_A^2}{k^2}, \tag{4.31}$$

where $K^2 = K_y^2 + K_z^2 + 1/4$, $\omega_g^2 = g/H$. Clearly, the third, new resonance is caused by the coupling of the magnetorotational and Parker instabilities.

The another feature of the eigenmodes of the coupling instability is the eigenmodes are no longer confined between two Alfvén singularities. As shown above, we can decompose the eigenmodes into the Fourier modes in the x direction if the background flow does not have shear, indicating the eigenmodes have infinite structure in the x direction. Thus, the eigenmodes 'leak' from the Alfvén singular points in both positive and negative x directions, destabilizes fluid to convection from boundary and g.

4.3 Discussion

The coupling of the magnetorotational and Parker instabilities has been discussed. The wave equation is derived by assuming the background shear flow and gravity, and the resonance and mode coupling of the Alfvén and Brunt-Väisälä frequency are shown. Since incompressibility is assumed, fluid is always unstable to convection. The dispersion relation shows that the shear flow does not stabilizes the Parker instability.

Magnetic field plays an important role in this coupled instability. Eq. (4.31) shows that the magnetic field parallel to the direction of the wave stabilizes the Parker instability, since the perturbation stretches the magnetic field line. The Alfvén frequency and Brunt-Väisälä frequency are coupled because of the magnetic field, which create another continuum.

General property of the eigenmodes is briefly examined by comparing two limit cases. In the pure magnetorotational case, as shown in Chapter 2, the eigenmode is sandwiched between two Alfvén singularities. However, in the pure Parker case, eigenmodes are not bounded. Thus, the eigenmode of the coupled instabilities increases its radial size with g.

Chapter 5

Conclusion

The magnetohydrodynamical structure formation of protoplanetary disks is studied. In Chapter 2, an accretion disk is shown to be unstable to non-axisymmetric perturbation of the magnetorotational instability. Since the magnetorotational instability transfers angular momentum out from an accretion disk and its eigenmodes create a structure in the radial direction, the result implies that magnetorotational eigenmodes construct the radial structure in the disk, which accelerates the planet formation prior to self-gravitation.

The another possible mechanism of planetary formation without self-gravitation of gas is discussed in Chapter 3. Even if the magnetization of a protoplanetary disk is weak at the very beginning of the planetary formation, magnetic field is continuously enhanced by the magnetorotational instability in the outer region. In the inner region, however, magnetic fields enhanced by kinematic dynamo are extracted from the disk surface via the Parker instability, which may cause the ejection of jets from the central region. The dominance of the magnetorotational instability in the early stage also implies that the radial structure in an accretion disk evolves faster than the azimuthal structure, creating ring-like structures in the disk first.

In the later(moderately magnetized) stage, all the three instabilities

compensate with each other, creating a disk turbulent in both the radial and azimuthal directions. Kinematic dynamo, driven by the central star in this stage, creates the radial structure in the inner region. Three dimensional simulation has shown that the arm and blob-like structure are created in a local shearing box because of the coupling of the magnetorotational and Parker instabilities, indicating gas aggregation prior to self-gravitation in a protoplanetary disk. This scenario does not require self-gravitation, which is essential for the conventional theory of the planetary formation, and create dense regions much faster than self-gravity. Since one of the most difficult problems from observations is that the planetary formation should be faster than the conventional theory, this scenario may solve this problem.

The radial mass spectra created by the magnetorotational instability, kinematic dynamo, and self-gravitation are estimated by assuming two types of the density profiles. The Spectrum with the torus density profile model has a maximum at some radius, which may explain the existence of huge mass extrasolar planets like Jupiter, and the origin of the Solar system. Since the magnetorotational instability is dominant in the early stage, the radial structure is created mainly caused by the excitation of eigenmodes of the magnetorotational instability. The structure is accentuated further accumulated by the Parker instability in the azimuthal direction and the Jeans instability in the later stage of the formation process. Since the maximum density radius can move with changing parameters in the potential model, these density spectra may explain the variety of the observed mass spectra of exosolarplanets.

The applicability of the shear-flow induced structure in laboratory plasma is discussed in place of the direct measurement of the magnetic viscosity in ac-

cretion disks. Even though the coupling of the magnetorotational instability or kinematic dynamo with the Parker instability may be weak in both a tokamak plasma and laser plasma, laboratory experiments may be achievable and useful for understanding the formation mechanism of planets and AGNs. Issues for achieving laboratory plasma experiments are addressed, which include control of sheared flow, radiation pressure, and inhomogeneity. Even though the schematics for these simulation experiments are ideal, these experiments may provide more information than computer simulations.

The coupling of the magnetorotational and Parker instabilities is analyzed. These two instabilities are coupled via magnetic field, which appears the coupling of the Alfvén frequency and the Brunt-Väisälä frequency explicitly. The wave equation is shown to be identical to the pure magnetorotational case if the gravitational effect is neglected. A detailed study of eigenmodes of this coupling instability remains to be an issue of investigation.

Bibliography

[1] T. Tajima and K. Shibata, *Plasma Astrophysics* (Addison Wesley, 1997), Chap. 3

[2] J. K. Cannizzo, A. W. Shafer and J. C. Wheeler, Astrophys. J. **333**, 227(1988).

[3] E. P. Velikhov, Sov. Phys. JETP, **35** 995(1959).

[4] S. Chandrasekhar, *Hydrodynamic and Hydromagnetic Stability* (Oxford: Clarendon, 1961), p384

[5] S. A. Balbus and J. F. Hawley, Astrophys. J. **376**, 214(1991).

[6] R. Matsumoto and T. Tajima, Astrophys. J. **445**, 767 (1995).

[7] M. J. LeBrun, T. Tajima, M. G. Gray, F. Furnish, and W. Horton, Phys. Plasmas **5**, 752(1993).

[8] H. Mizuno, Prog. Theor. Phys. **64**, 544(1980).

[9] J. B. Pollack, Annu. Rev. Astron. Astrophys. **22**, 389(1984).

[10] J. J. Lissauer, Icarus **69**, 249(1987).

[11] G. W. Wetherill, Annu. Rev. Earth Planet. Sci. **18**, 205(1990).

[12] G. W. Wetherill, Icarus **119**, 219(1996).

[13] A. P. Boss, Astrophys. J. **536**, L101(2000).

[14] J. F. Hawley, Astrophys. J. **528**, 462(2000).

[15] M. Machida, M. R. Hayashi and R. Matsumoto, Astrophys. J. Lett. **532**, L67 (2000).

[16] E. N. Parker, Astrophys. J. **145**, 811(1966).

[17] E. N. Parker, *Cosmical Magnetic Fields* (Clarendon Press, Oxford, 1979), p325.

[18] E. N. Parker, Astrophys. J. **162**, 665(1970).

[19] T. F. Stepinski and E. H. Levy, Astrophys. J. **362**, 318(1990).

[20] R. M. Kulsrud and S. W. Anderson, Astrophys. J. **396**, 606(1992).

[21] M. V. Rekowsky, G. Rüdiger, and D. Elstner, Astron. Astrophys. **353**, 813(2000).

[22] R. Okada, J. Fukuke and R. Matsumoto, Publ. Astron. Soc. Japan **41**, 133(1989).

[23] W. T. Kim and E. C. Ostriker, Astrophys. J. **540**, 372(2000).

[24] C. Terquem and J. C. B. Papaloizou, Man. Not. R. Astron. Soc. **279**, 767(1996).

[25] D. N. C. Lin and J. C. B. Papaloizou, Man. Not. R. Astron. Soc. **191**, 37(1980).

[26] A. E. Gill, *Atmosphere-ocean dynamics*(New York: Academic Press, 1982), p52

[27] W. Kley, J. C. B. Papaloizou, and D. N. C. Lin, Astrophys. J. **416**, 679(1993).

[28] J. C. B. Papaloizou and J. E. Pringle, Man. Not. R. Astron. Soc. **208**, 721(1984).

[29] S. Kato, Publ. Astr. Soc. Jpn. **39**, 645(1987).

[30] W. Gratzel, Mon. Not. R. Astr. Soc. **225**, 227(1987).

[31] D. M. Eardley and A. P. Lightman, Astrophys. J. **200**, 187(1975).

[32] S. Ichimaru, Astrophys. J. **208**, 701(1977).

[33] R. E. Pudritz, Mon. Not. R. Astr. Soc. **195**, 881(1981).

[34] S. Kato, Publ. Astr. Soc. Jpn. **36**, 55(1984).

[35] S. Kato and T. Horiuchi, Publ. Astr. Soc. Jpn. **37**, 399(1985).

[36] S. Kato and T. Horiuchi, Publ. Astr. Soc. Jpn. **38**, 313(1986).

[37] E. T. Vishniac and P. Diamond, Astrophys. J. **347**, 447(1989).

[38] M. Rozyczka and H. C. Spruit, Astrophys. J. **417**, 677(1993).

[39] D. Ryu and J. Goodman, Astrophys. J. **338**, 438(1992).

[40] W. Cabot and J. B. Pollack, Geophys. Astrophys. Fluid Dyn. **64**, 97(1992).

[41] J. M. Stone and S. A. Balbus, Astrophys. J. **464**, 364(1996).

[42] S. P. Ruden and J. B. Pollack, Astrophys. J. **375**, 740(1991).

[43] M. Kaisig, Astron. Astrophys. **218**, 89(1989).

[44] J. F. Hawley and S. A. Balbus, Astrophys. J. **376**, 223(1991).

[45] J. F. Hawley, C. F. Gammie and S. A. Balbus, Astrophys. J. **440**, 742(1995).

[46] S. Kumar, C. S. Coleman, and W. Kley, Mon. Not. R. Astron. Soc. **266**, 379(1994).

[47] J. F. Hawley and S. A. Balbus, Astrophys. J. **400**, 595(1992).

[48] R. Matsumoto, A. Valinia, T. Tajima, K. Makishima, and K. Shibata, Adv. Space Res. **25**, 499(2000).

[49] S. A. Balbus and J. F. Hawley, Astrophys. J. **400**, 610(1992).

[50] G. I. Ogilvie, and J. E. Pringle, Mon. Not. R. Astron. Soc. **279**, 152(1996).

[51] A. Hasegawa and L. Chen, Phys. Fluids **19**, 1924(1976).

[52] C. Z. Cheng and M. S. Chance, Phys. Fluids **29**, 3695(1986).

[53] T. Tajima, W. Horton, P. J. Morrison, J. Schutkeker, T. Kamimura, K. Mima, and Y. Abe, Phys. Fluids **B3**, 938(1991).

[54] K. Noguchi, T. Hatori, and T. Kato, J. Phys. Soc. Jpn. **67**, 1250(1998).

[55] P. M. Morse, and H. Feshbach, *Methods of Theoretical Physics* (McGraw-Hill: New York), p532(1953).

[56] Z. Yoshida and M. Mahajan, International J. Mod. Phys. B **22** 2857(1995).

[57] H. William *et al.*, *Numerical recipes in FORTRAN : the art of scientific computing* (Cambridge University Press), (1992).

[58] G. W. Marcy and R. P. Butler, Publ. Astron. Soc. Pac. **112**, 137 (2000).

[59] S. J. Wolk and F. M. Walter, Astron. J. **111**, 2066(1996).

[60] R. Jayawardhana, *et al.*, Astrophys. J. **521**, L129(1999).

[61] J. Bally, L. Testi, A. Sargent, and J. Carlstom, Astron. J. **116**, 854(1998).

[62] M. Harwit, *Astrophysical Concepts*, 3rd Edition (Springer, 1998), p31

[63] K. Noguchi, T. Tajima and R. Matsumoto, Astrophys. J. **541**, 802 (2000).

[64] G. W. Marcy and R. P. Butler, *The Origin of Planetary Systems* (Klawer Academic Publishers, 1999), p681.

[65] A. Cumming, G. W. Marcy and R. P. Butler, Astrophys. J. **526**, 890 (1999).

[66] A. P. Boss, Astrophys. J. **503**, 923(1998).

[67] A. P. Boss, Science **276**, 1836(1997).

[68] H. M. J. Boffin, S. J. Watkins, A. S. Bhattal, N. Francis, and A. P. Whitworth, Man. Not. R. Astron. Soc. **300**, 1189(1998).

[69] W. J. Nellis, M. Ross and N. C. Holmes, Nature **269**, 1249 (1995).

[70] S. T. Weir, A. C. Mitchell and W. J. Nellis, Phy. Rev. Lett. **76**, 1860(1996).

[71] W. J. Nellis, Sci. Am. **282**, 84(2000).

[72] J. B. Pollack, O. Hubickyj, P. Bodenheimer, J. J. Lissauer, M. Podolak, and Y. Greenzweig, Icarus **124**, 62(1996).

[73] T. D. Swindle, Protostars and Planets III, edited by E. H. Levy and J. I. Lunine, (Tuscon : University of Arizona Press, 1993), p867.

[74] A. P. Boss, *ORIGINS*, edited by C. E. Woodward, J. M. Shall and H. A. Thronson (ASP Conference Series, 1998), Vol. 148, P314.

[75] P. Zhu and W. Horton, Phy. Plasmas **6**, 2503(1999).

[76] W. Horton, R. A. Smith, J. Geophys. Res. **93**, 12761(1988).

[77] D. Ryutov, *et al.*, Astrophys. J. **518**, 821(1999).

[78] K. Shibata *et al.*, Astrophys. J. **338**,471(1989).

[79] K. Shibata and R. Matsumoto, Science **353**, 633(1991).

[80] S. Narita, C. Hayashi and S. M. Miyama, Prog. Theor. Phys, **72**, 1118(1984).

[81] W. Chou, Ph.D. Dissertation, UT-Austin(1998).

[82] W. Chou, R. Matsumoto, T. Tajima, M. Umekawa and K. Shibata, Astrophys. J. **538**, 710(2000).

[83] D. R. Ernst, R. E. Bell, M. G. Bell, R. V. Budny, B. Coppi, G. W. Hammett, R. J. Hawryluk, K. W. Hill, D. K. Mansfield, D. R. Mikkelsen, H. K. Park, M. Porkolab, S. D. Scott, G. L. Schmidt, E. J. Synakowski, and M. C. Zarnstorff, the TFTR Group, Phys. Plasmas,**7**, 615(2000).

[84] K. H. Burrell, E. J. Doyle, P. Gohil, R. J. Groebner, J. Kim, R. J. LaHaye, L. L. Lao, R. A. Moyer, T. H. Osborne, W. A. Peebles, C. L. Rettig, T. H. Rhodes and D. M. Thomas, Phys. Plasmas, **1**, 1536(1994).

[85] W. L. Rowan, A. G. Meigs, E. R. Solano and P. M. Valanju, Phys. Fluids **5**, 2485(1993).

[86] F. W. Perkins, R. B. White, P. T. Bonoli, and V. S. Chan, in Eighteenth Fusion Energy Conference Proceedings, Srrento, Italy, 2000, IAEA-CN-77/TH1/1.

[87] D. Ryutov, Comm. Plasma Phys. Contr. Fus., **17** 1(1995).

[88] R. D. Hazeltine and J. D. Meiss, Phys. Reports **121**, 137(1985).

[89] C. Z. Cheng, L. Chen, and M. S. Chance, Ann. Physics **161**,21(1985).

[90] A. Fasoli *et al.*, Phys. Rev. Lett. **75**, 645(1995).

[91] K. L. Wong *et al.*, Plasma Phys. Control. Fusion **36**, 879(1994).

[92] W. Horton, Rev. Mod. Phys. **71**, 735(1999).

[93] B. Copi, *et al.*, in Eighteenth Fusion Energy Conference Proceedings, Srrento, Italy, 2000.

[94] L. Colas, *et al.*, Nucl. Fusion **38**, 903(1998).

[95] J. S. Greaves, *et al.*, Astrophys. J. **506**, L133(1998).

[96] C. W. Horton and Y. H. Ichikawa, *Chaos and structures in nonlinear plasmas* (World Scientific, 1996), Chap. 4.

[97] J. S. Mathis, W. Rumpl and K. H. Nordsieck, Astrophys. J. **217**, 425 (1977).

[98] L. S. Spitzer, *Physical Processes in the Interstellar Medium* (Wiley-Interscience, 1978).

[99] D. A. Mendis and M. Rosenberg, Ann. Rev. Astron. Astrophys. **32** 419 (1994).

[100] L. I. Rudakov, *Physica Scripta* (in press)(2000).

[101] T. Nakano, Publ. Astron. Soc. Japan **34**, 337(1982).

[102] W. Horton, and P. Zhu, Phys. Plasmas **7**, 4534(2000).

[103] J. E. Rice, *et al.*, Phys. Plasmas **7**, 1825(2000).

[104] I. H. Hutchinson, *et al.*, Phys. Rev. Lett. **84**, 3330(2000).

Vita

Koichi Noguchi was born in Tokyo, Japan on April 18, 1972, the second child of Yoji and Reiko Noguchi. After graduating from Waseda High School in 1991, he entered the Waseda University majoring in Applied Physics, and received the degree of Bachelor of Engineering in March, 1995. He then entered the Graduate School at the Waseda University majoring in Physics, and received the degree of Master of Science in March, 1997. He entered the Graduate School in the Department of Physics at the University of Texas at Austin in the fall of 1997. Since then he has been employed as a teaching assistant by the Department of Physics and as a graduate research assistant by the Institute for Fusion Studies.

Permanent address: 2-11-3 Sanno
Ota-ku Tokyo, 143-0023
Japan

This dissertation was typeset with LaTeX2e[†] by the author.

[†]LaTeX2e is an extention of LaTeX. LaTeX is a collection of macros for TeX. TeX is a trademark of the American Mathematical Society. The macros used in formatting this dissertation were written by Dinesh Das, Department of Computer Sciences, The University of Texas at Austin.